JGR Oceans

RESEARCH ARTICLE
10.1029/2022JC018668

# Validating Finescale Parameterizations for the Eastern Arctic Ocean Internal Wave Field

**Till M. Baumann[1,2], Ilker Fer[1], Kirstin Schulz[3], and Volker Mohrholz[4]**

[1]Bjerknes Centre for Climate Research, University of Bergen, Bergen, Norway, [2]Now at Institute for Marine Research, Bergen, Norway, [3]Oden Institute for Computational Engineering and Sciences, The University of Texas at Austin, Austin, TX, USA, [4]Leibniz Institute for Baltic Sea Research, Warnemünde, Germany

**Key Points:**

- Comparisons to in-situ measurements show that Finescale Parameterization (FS) is applicable over a wide range of eastern Arctic conditions
- Energy content and shape of the spectra describing the internal wave field may indicate whether conditions are suitable for FS
- For the strain-only formulation of FS, a shear-strain ratio of 7 appears to be representative of eastern Arctic conditions

**Correspondence to:**
T. M. Baumann,
till.baumann@hi.no

**Citation:**
Baumann, T. M., Fer, I., Schulz, K., & Mohrholz, V. (2023). Validating finescale parameterizations for the eastern Arctic Ocean internal wave field. *Journal of Geophysical Research: Oceans*, *128*, e2022JC018668. https://doi.org/10.1029/2022JC018668

Received 23 MAR 2022
Accepted 15 OCT 2023

**Author Contributions:**

**Conceptualization:** Till M. Baumann, Ilker Fer
**Data curation:** Till M. Baumann, Ilker Fer, Kirstin Schulz, Volker Mohrholz
**Formal analysis:** Till M. Baumann
**Investigation:** Till M. Baumann
**Methodology:** Till M. Baumann, Ilker Fer
**Supervision:** Ilker Fer
**Writing – original draft:** Till M. Baumann, Ilker Fer
**Writing – review & editing:** Till M. Baumann, Ilker Fer, Kirstin Schulz, Volker Mohrholz



**Abstract** In the Arctic Ocean, vertical transport of heat by turbulent mixing is ultimately coupled to the sea-ice cover, with immediate and far-reaching impacts on the climate and ecosystem. Unfortunately, direct observations of mixing are difficult, expensive and sparse. Finescale Parameterization (FS) of turbulent energy dissipation rate ($\varepsilon$) allows for the quantification of turbulence from breaking internal waves using standard measurements, such as profiles of hydrography and velocity. While FS proved to be reliable in mid-latitudes, the Arctic Ocean internal wave field is distinct in terms of composition and energy level, rendering the applicability of FS uncertain. To test FS in a wide range of eastern Arctic conditions, we compiled data from eight cruises. All profiles used to calculate FS were collocated with in-situ measurements of $\varepsilon$ obtained from microstructure profilers. FS was applied between 50 and 450 m below the surface. Results show a satisfactory performance of FS, with 84% of FS-derived $\varepsilon$ being within a factor of 5 to observations. This improved to 90% when using lower-noise velocity profiles of lowered current meters instead of ship-mounted current meters. In our data, FS performance is independent of the shear-strain ratio ($R_\omega$) and internal wave field bandwidth ($N/f$), but there is evidence that highly stratified environments with large potential energy, low turbulence and substantially non-white shear spectra are less suitable for FS. A widely used formulation of FS using only hydrography and a prescribed $R_\omega = 7$ results in 73% of FS estimates being within a factor of 5 to observations.

**Plain Language Summary** Turbulent mixing of water masses can redistribute heat in the ocean. This is especially important in the Arctic Ocean, where turbulent transport of heat from the relatively warm interior could reach the cold surface waters and thus melt sea ice. Unfortunately, direct observations of turbulence are complicated and expensive and therefore sparse. However, turbulence at centimeter scales induced by breaking internal waves can be estimated from standard observations of ocean current and density profiles measured at $\mathcal{O}(10)$ m scales, using finescale parameterization (FS). FS was designed for the mid-latitudes in environments and internal wave fields distinct from the Arctic and it is unclear if the method works well in the Arctic. We use data from eight Arctic cruises that performed standard observations together with direct measurements of turbulence. This enables us to test FS and compare the results to direct measurements. We find that 84% of FS-derived values for the dissipation rate $\varepsilon$ are within a factor of 5 to observations. This is a fairly good agreement for turbulence measurements and indicates that FS is applicable in Arctic environments. However, we also identified some specific conditions that may be less suitable for FS.

## 1. Introduction

Mixing processes play a central role in shaping the Arctic Ocean's water masses and circulation (e.g., Holloway & Proshutinsky, 2007; Lenn et al., 2022; Timmermans & Marshall, 2020). The warm subsurface waters originating from the Atlantic and Pacific Oceans form a considerable heat reservoir in the Arctic Ocean, sufficient to melt all Arctic sea ice several times over (e.g., Turner, 2010). Under climate change, this reservoir is likely to grow as heat transports from the Atlantic and Pacific Oceans into the Arctic are projected to increase (e.g., Dörr et al., 2021). For subsurface oceanic heat to reach the surface, and sea ice, vertical mixing must take place. Turbulent mixing further affects the redistribution of nutrients, carbon, oxygen and other dissolved gasses (Randelhoff et al., 2020; Schulz et al., 2022a). Quantifying spatio-temporally varying mixing processes in the Arctic is thus key to understanding and accurately projecting the changing Arctic Ocean state. Consequently, substantial efforts have been devoted to the study of Arctic mixing, but due to the complexity of microstructure measurements, turbulence data remain sparse and scattered.

The strongest mixing events recorded in the Arctic Ocean are localized in space and episodic in time, driven by tidal currents impinging on particular topographic features or atmospheric storms creating divergent currents and ice drift at the surface (e.g., McPhee et al., 2005; Meyer, Fer, Sundfjord, & Peterson, 2016; Padman & Dillon, 1991). Relatively less energetic mixing occurs ubiquitously in the ocean interior due to the breaking of internal waves that are continuously generated by tides and wind. Even modest mixing creating heat fluxes of $\mathcal{O}(1)$ W m$^{-2}$ can have a substantial impact on the balance of the perennial sea ice cover (Carmack et al., 2015).

Compared to lower latitudes, energy levels of the Arctic internal wave field have been reported to be quite low (Levine et al., 1987; Pinkel, 2008); hence, the resulting mixing is expected to be comparably weak. However, a receding sea-ice cover could facilitate a more efficient transfer of momentum from the atmosphere into the ocean, energizing the inertial wave field. Enhanced near-inertial currents were observed under ice-free conditions (Polyakov et al., 2020; Rainville & Woodgate, 2009), suggesting that the Arctic Ocean is transitioning to a more energetic future. We note, however, that hitherto no substantial trends in the internal wave field energy have been observed (Dosser & Rainville, 2016; Guthrie et al., 2013), indicating that the Arctic internal wave field may not only be suppressed by the presence of sea ice but possibly also by the inefficient transmission of near-inertial energy from the surface through the relatively shallow Arctic surface mixed layer (SML) boundary (Guthrie & Morison, 2021).

"Background" mixing originating from the internal wave field can be predicted from larger scale [vertical scales O(10–100 m)] observations and does not require specialized microstructure measurements. This is done via the finescale parameterization (FS) that was developed by Gregg (1989) and later generalized by Polzin et al. (1995) and has been extensively used ever since (see Polzin et al., 2014, for a review). Practically, this method is based on assessing the properties of the internal wave field in terms of observed velocity shear and/or strain and comparing them to the empirical Garrett & Munk ("GM," Garrett & Munk, 1975) model of the background internal wave continuum. FS predicts the turbulent dissipation rate $\varepsilon$, assuming the internal wave energy at finescale cascades down to smaller scales through weakly nonlinear interactions. A successful and reliable application of FS can allow a better mapping and quantification of the distribution of background mixing using relatively widespread measurements of ocean currents and hydrography. Mixing rates can then be used to estimate the redistribution of heat and, for example, nutrients in the Arctic. However, since the GM model is based on mid-latitude observations, its applicability to the Arctic Ocean internal wave field is somewhat uncertain (see discussions in Polzin et al., 2014; Fine et al., 2021).

The environmental conditions of the internal wave field in the Arctic Ocean can limit the applicability of FS. Freely propagating internal waves cannot exist poleward of their critical latitude, where $\omega < f$ (with the wave frequency $\omega$ and $f$ being the Coriolis parameter). The critical latitude for the dominant $M_2$ tidal waves is 74.5°N, rendering it sub-inertial over most of the Arctic domain. Consequently, the Arctic Ocean internal wave field is less energetic compared to mid-latitudes and is dominated by wind-driven Near-Inertial Waves (NIWs). A measure of the composition of the internal wave field is $R_\omega$, defined as the ratio between shear variance and strain variance. While in GM, this ratio is taken to be 3, global observations suggest an average value of $R_\omega = 7$ (Kunze et al., 2006). In the NIW dominated Arctic internal wave field produces highly variable, but generally higher values, often exceeding 10 (e.g., Fine et al., 2021). Furthermore, the synoptic nature of NIW-generating wind events can lead to substantial temporal variability of the internal wave field, thus violating the assumed steady state the non-linear spectral energy transfer is based on. This non-stationarity is exacerbated by the generally low internal wave energy level, yielding only small non-linear wave-wave interactions and thus prolonging the time it takes for a spectral continuum to form after the injection of NIW energy. Furthermore, FS may be biased in NIW-dominated domains due to the susceptibility of these long waves to either break directly or to interact with mesoscale eddies, thus not contributing to energy transfer as expected (e.g., Thomas & Zhai, 2021).

Past evaluations of FS in the Arctic Ocean are scarce and limited to regionally focused and short duration experiments. In an Arctic fjord in the Svalbard Archipelago, known for enhanced mixing and deep water formation, Fer (2006) compared direct observations of dissipation rate from several profiles with FS and found good agreement of $\varepsilon$ despite some spectral deviations from GM, with ratios between FS and observations ranging between 0.1 and 2, averaging 0.84. Near the marginal ice zone on the southern flanks of Yermak Plateau, where the energy of the internal wave field was 0.1–0.3 times the midlatitude levels, FS estimates agreed to within a factor of 2 of the directly observed station-averaged (over about 24 hr and ~40 casts) dissipation profiles (Fer et al., 2010). Guthrie et al. (2013) validated FS results from expendable current probes (XCP) and conductivity, temperature and depth (CTD) profiles from the Yermak Plateau and near the North Pole against microstructure casts, and they

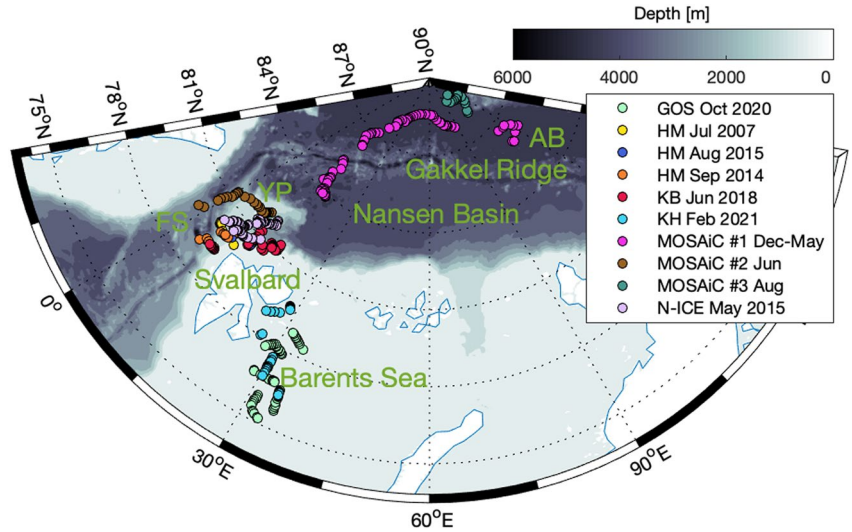


**Figure 1.** Map showing all hydrographic stations used in this study. Different cruises and different parts of the MOSAiC expedition are shown as colored dots. Key geographical features are labeled; FS, Fram Strait; YP, Yermak Plateau; AB, Amundsen Basin. Bathymetry stems from the International Bathymetric Chart of the Arctic Ocean (IBCAO) Version 4.0 (Jakobsson et al., 2020).

found good agreement, well within the known limitations of FS. Fine et al. (2021) validated FS using microstructure profiles from a 14.5 hr duration survey in the Beaufort Sea, and found that strain-based FS estimates were biased high relative to observations of $\varepsilon$ between 100 and 200 m by approximately a factor of four.

Performing FS in the absence of collocated velocity and CTD observations requires the choice of a fixed value for $R_\omega$. Guthrie et al. (2013) use a host of XCP and CTD profiles across the central Arctic to assess long term trends of turbulence using FS with a fixed $R_\omega$ value of 11. Fine et al. (2021) investigated temporal variability of internal wave-driven turbulence and related parameters using 8 days of moored observations in the Beaufort Gyre in an environment with highly variable shear-to-strain ratio, averaging 17 on a range between 3 and 50. Using moored observations and a fixed $R_\omega$ of 7, Chanona and Waterman (2020) investigated temporal variability of internal wave driven mixing at two Arctic locations: Nares Strait and in the Beaufort Sea. Dosser et al. (2021) used a fixed shear-to-strain ratio of 7 on pan-Arctic data from ice-tethered profilers spanning a period of 18 years.

In an effort to further investigate the applicability of FS in the context of the unique Arctic oceanographic conditions, we here bring together eight data sets of ocean microstructure, stratification and current profiles from the Arctic environment, geographically covering latitudes from 75°N to 89°N and longitudes from 2°W to 127°E to systematically apply and test FS. Despite the uncertainties of the approach for the Arctic conditions, FS in its widely applied form captures the directly observed turbulent energy dissipation rate $\varepsilon$ to within a factor of 5 in 84% of estimates.

## 2. Data and Methods

### 2.1. Cruise Selection

In this study, we use data from eight different cruises carried out in the regions of the Barents Sea, Fram Strait, Yermak Plateau and central Arctic (Figure 1, Table 1). Because of its duration of almost a year and large spatial coverage, we divide the MOSAiC expedition into its three separate drifts (Rabe et al., 2022). To facilitate a thorough investigation of the applicability of FS in these regions, we collate a set of trusted data covering a large range of values for the relevant parameters current shear, Brunt-Väisälä frequency (i.e., stratification) and dissipation rate of turbulent kinetic energy $\varepsilon$. Figure 2 shows cruise-averaged profiles of these parameters, each range over more than two orders of magnitude at depths between 50 and 450 m.

### 2.2. Observed Profiles

Vertical profiles of horizontal velocity shear were obtained from ship-mounted acoustic Doppler current profilers (SADCPs) and/or lowered ADCPs (LADCPs). While the SADCPs are mounted in the ship's hull and operate

**Table 1**
*Details of the Data Used in This Study*

| Name | SADCP (kHz) | LADCP (kHz) | Period (Start–End) | Region | Profiler | Casts count | Depth range (m) | Data set reference |
|---|---|---|---|---|---|---|---|---|
| GOS Oct 2020 | 75 | 300 | 14.10.2020–24.10.2020 | Barents Sea | MSS | 153 | 60–180 | Fer et al. (2021) |
| HM Jul 2007 | 75 | – | 23.07.2007–30.07.2007 | NW Svalbard | MSS | 79 | 100–350 | Fer et al. (2010) |
| HM Aug 2015 | 75 | 300 | 14.10.2015–19.10.2015 | NW Svalbard | VMP | 56 | 100–400 | Fer and Kolås (2018) |
| HM Sep 2014 | 75 | 300 | 08.09.2014–12.09.2014 | NW Svalbard | VMP | 35 | 70–450 | N/A |
| KB Jun 2018 | 150 | 300 | 29.06.2018–08.07.2018 | N Svalbard | VMP | 110 | 70–330 | Fer, Koenig, Bosse, et al. (2020) |
| KH Feb 2021 | 150 | 300 | 13.02.2021–26.02.2021 | Barents Sea | MSS | 83 | 50–200 | Nilsen et al. (2021) |
| MOSAiC #1 Dec–May | 75 | – | 23.12.2019–07.05.2020 | Central Arctic | MSS | 446 | 100–250 | Baumann et al. (2021) and Schulz et al. (2022c) |
| MOSAiC #2 Jun | 75 | – | 27.06.2020–26.07.2020 | YP & FS | MSS | 193 | 100–330 | Baumann et al. (2021) and Schulz et al. (2022c) |
| MOSAiC #3 Aug | 75 | – | 28.08.2020–18.09.2020 | Central Arctic | MSS | 117 | 50–200 | Baumann et al. (2021) and Schulz et al. (2022c) |
| N-ICE May 2015 | 75 | – | 03.05.2015–18.06.2015 | YP | MSS | 337 | 100–300 | Meyer, Fer, Sundfjord, Peterson, Smedsrud, et al. (2016) and Provost et al. (2016) |

*Note*. "Depth range" refers to the depth interval over which Finescale Parameterization (FS) was applied. Capital letters before region names denote geographic direction (N = North, etc.), other abbreviations are the same as in Figure 1. The makes of the microstructure profilers ("Profiler") are either Sea & Sun Microstructure Probe (MSS) or Rockland Scientific Vertical Microstructure Profilers (VMP).

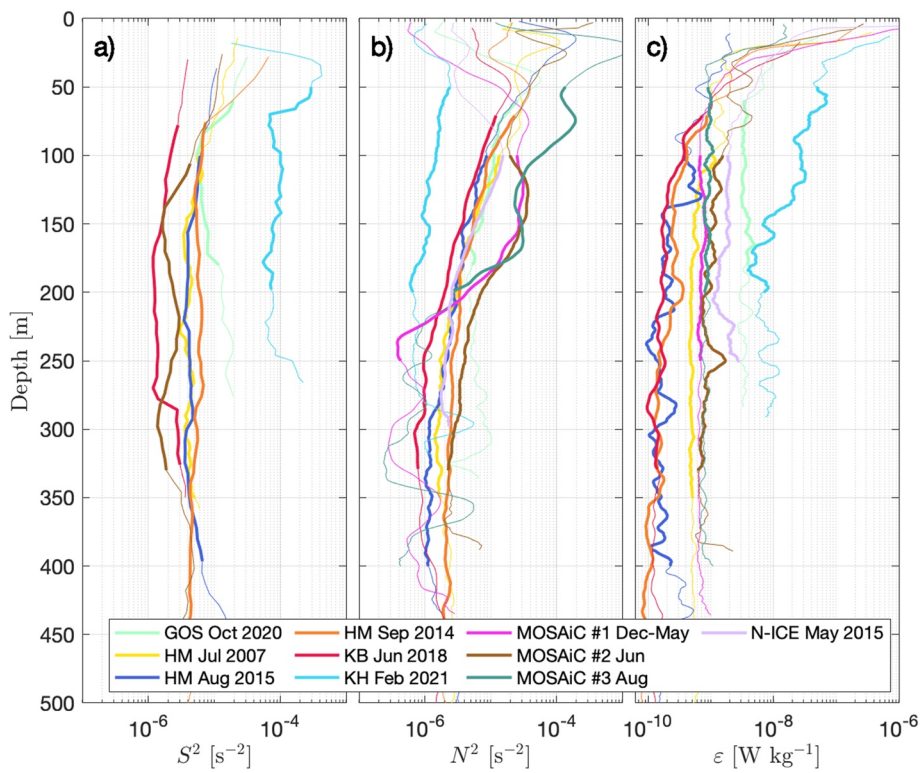


**Figure 2.** Profiles of shear squared $\left(S^2 = \left(\frac{\partial u}{\partial z}\right)^2 + \left(\frac{\partial v}{\partial z}\right)^2\right)$, Brunt-Väisälä frequency squared ($N^2$) and turbulent energy dissipation rate ($\varepsilon$) geometrically averaged over each cruise and smoothed with a 9-m sliding average. While arithmetic means were used for the Brunt-Väisälä frequency squared, the dissipation rate and shear squared were averaged using a geometric mean, to account for their approximately log-normal distribution in nature. The thick portion of the lines indicates depth ranges used for Finescale parameterization (FS), as indicated in Table 1.

continuously during the cruise, the LADCPs are fixed to the CTD frame and are deployed at stations. For the MOSAiC and N-ICE campaigns, we use data from ADCPs that were deployed away from the ship through a hole drilled into the ice floe and moored just beneath the ice. The under-ice ADCPs have a higher vertical resolution and lower noise levels compared to SADCPs. Due to their quasi-continuous sampling, we classify them as SADCPs in the remainder of this study. All SADCP profiles were bin-averaged to 1-hr time resolution. For a robust application of FS, it is advantageous to have a high vertical resolution of all measured parameters, thus we only use velocity profiles with a vertical resolution of 8 m or better.

Hydrographic profiles (temperature, salinity, potential density) were obtained together with direct observations of the turbulent energy dissipation rate $\varepsilon$ from free-falling microstructure profilers of the makes MSS (from Sea & Sun Technology, Germany) or Vertical Microstructure Profilers (VMP) (from Rockland Scientific, Canada). Typical vertical resolution after processing is 0.5–2 m. For the unpumped sensors of the MSS, salinity is obtained after correcting for the lag between temperature and conductivity measurements.

The manifestation of internal waves in hydrographic profiles is assessed using *strain*, the vertical gradient of vertical isopycnal displacement that can be estimated as

$$\zeta_z = \frac{N^2(z) - N_{bg}^2(z)}{\overline{N^2}}, \tag{1}$$

where the squared Brunt-Väisälä frequency is approximated as $N^2 = \frac{-g}{\rho_0}\frac{\partial \sigma_0}{\partial z}$, with the acceleration due to gravity $g = 9.81$ m s$^{-2}$, profile-average density $\rho_0$ and the sorted potential density anomaly, $\sigma_0$, referenced to surface pressure. An overbar denotes vertical averaging over the analysis segment and $N_{bg}$ is the background stratification. Similar to Polzin et al. (1995), the background state is approximated by a third order polynomial fit to the observed profile in the chosen depth interval. For further analysis, each strain and dissipation profile is paired with the velocity profile closest in time with a maximum allowed time difference of 2 hr.

### 2.3. Noise Level of Microstructure Observations

Over large parts of the interior ocean, turbulence is so weak that it is difficult to measure (i.e., it may be indistinguishable from the noise generated by the instrument). The noise level sets the lowest detection level of the dissipation rate. While MSS and VMP both use shear probes to determine $\varepsilon$ (cf. Fer et al., 2010; Fer, Koenig, Kozlov, et al., 2020), the noise levels for $\varepsilon$ estimates of the instruments are different. The manufacturers do not provide expected noise levels in dissipation rate units for these kinds of probes. Based on extensive experience with both kinds of instruments (see also the respective data set references in Table 1), we set the expected noise level to the (conservative) values of $1 \times 10^{-10}$ W kg$^{-1}$ for the VMP and $2 \times 10^{-9}$ W kg$^{-1}$ for MSS (for context, lower noise levels of $10^{-11}$ W kg$^{-1}$ for the VMP (e.g., Fer et al., 2018) and $10^{-9}$ W kg$^{-1}$ for the MSS (e.g., Schulz et al., 2022c) are common in literature). In low-turbulence environments, the noise level can create a high-bias in the measurements. Removing all data near the noise level would exclude most of the data and bias the data set toward energetic turbulence events. Instead, we make use of the near log-normal nature of $\varepsilon$ and fit a log-normal probability distribution function (pdf) to the part of distribution of measured $\varepsilon$ values that is above the noise level (with the mean, $\mu$, and standard deviation, $\sigma$, of the pdf as free parameters, similar to Fer et al. (2014)). Although recent insights suggest ocean turbulence is more accurately captured by log-skew-normal distributions (Cael & Mashayek, 2021), we find that, for the present application, fits of log-skew-normal distributions (with "skewness" as third free parameter) are less robust than those of log-normal distributions. While both geometric and arithmetic averaging can be used, they result in different interpretations of the dissipation rate: the former robustly represents typical values of $\varepsilon$ whereas the latter is heavily weighted toward high values of $\varepsilon$ and arguably more representative of the average total dissipation which disproportionately depends on individual highly dissipative events (e.g., Scheifele et al., 2018). With a focus on dissipation rates associated to the background internal wave field, in this study we deem the geometric mean to be the appropriate representation of average values of $\varepsilon$. Since for any individual profile, the number of $\varepsilon$ values above the noise level can be small and does not consistently allow for robust fits, we first group $\varepsilon$ profiles based on their location (given as x-y coordinates on a stereographic projection) and timing (given as decimal days) using a k-means clustering algorithm. The number of clusters is chosen so that on a cruise average, 10–15 casts are grouped together. For each cluster, a log-normal pdf is then fitted to the part of the distribution above the set noise level, yielding an estimate for average $\varepsilon$ that is not limited by noise, which is then used for comparison to FS-derived $\varepsilon$ (Figure 3).

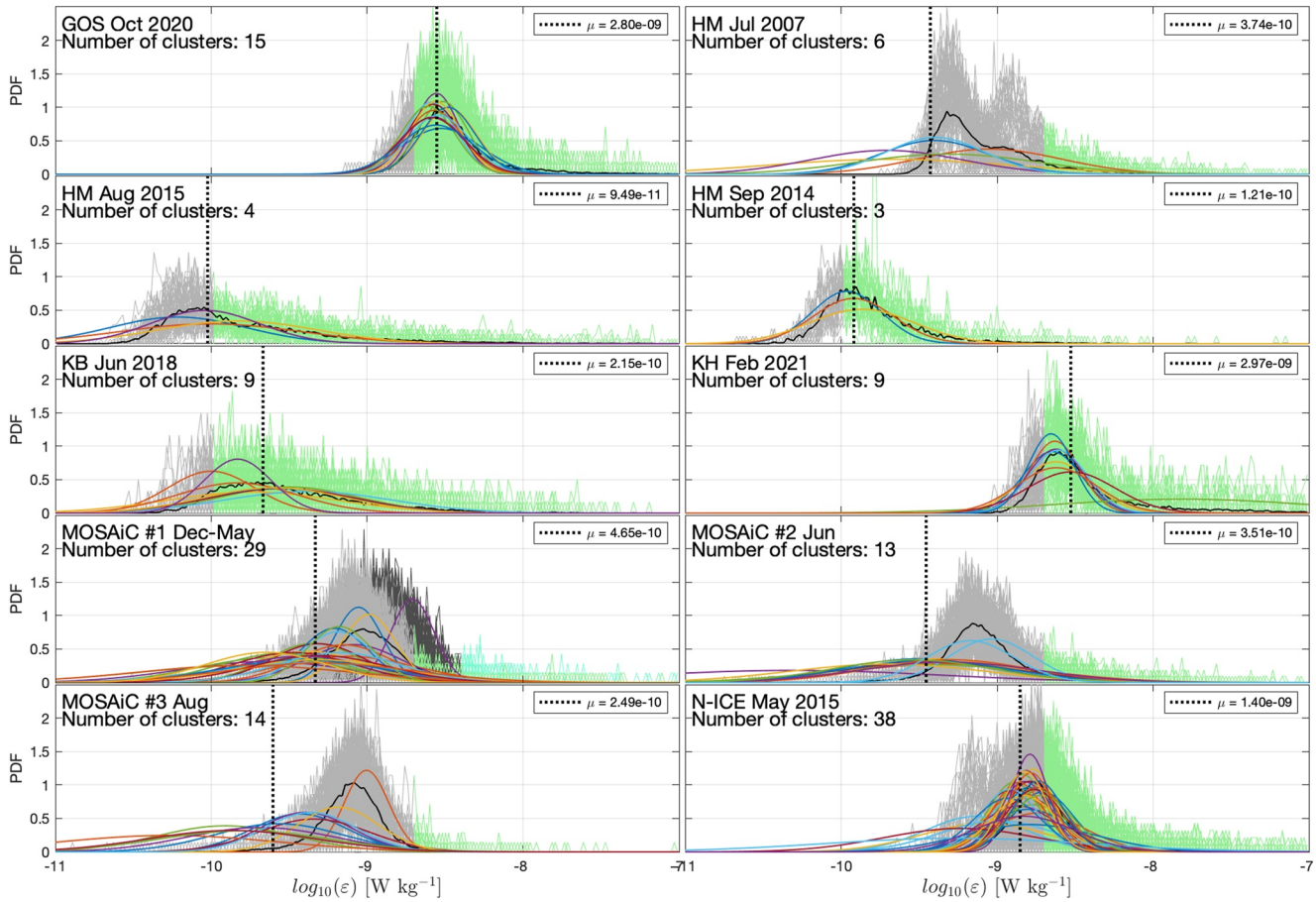


**Figure 3.** Probability distribution functions (pdf) of all $\varepsilon$ profiles associated with ship-mounted acoustic Doppler current profiler profiles for each cruise. The parts of the distribution above the instrument-dependent noise level are marked in green ($2 \times 10^{-9}$ W kg$^{-1}$ for MSS and $1 \times 10^{-10}$ W kg$^{-1}$ for Vertical Microstructure Profilers). Due to an observed increase in the noise level after a probe change during MOSAiC #1, we use a higher noise level ($4 \times 10^{-9}$ W kg$^{-1}$) for all $\varepsilon$ after the probe change (dark gray and teal distributions). The pdf of all data per cruise (including those below noise level) is shown in black. Colored lines show the log-normal distributions for each cluster (see text) fitted to the part of the distribution above the noise level. The dotted black line indicates the geometric average of all mid-points of the fitted distributions.

The clustering effectively averages microstructure measurements over similar time and space scales as those underlying FS theory (i.e., the interaction of internal waves of different origins), thus conforming to the best practices for comparing $\varepsilon$ values as outlined by Whalen (2021).

### 2.4. Shear and Strain Variances From Spectral Analysis

Vertical wavenumber spectra of shear and strain are obtained by performing Fourier transforms on the individual profiles. Instead of using first-differenced velocity profiles, shear spectra were obtained directly from velocity spectra:

$$\Psi_{shear} = (2\pi k)^2 \Psi_{vel}, \tag{2}$$

where $k$ is the cyclic vertical wavenumber vector and $\Psi_{vel}$ is the sum of spectra of the two horizontal components of velocity. Variances are then obtained by integrating the vertical wavenumber spectra for shear and strain. However, the process is not trivial and involves several decisions with varying degrees of objectivity that impact the final results. To facilitate reproducibility, we here outline decisions and procedures applied in the processing.

- Depth range: The depth range for FS application was visually determined for each cruise from the vertical data coverage and apparent SML depth. The goal is to use the longest continuous vertical span of data outside the SML and other "undesirable" regions (see below). We only included profiles whose deepest measurements

equaled or exceeded the maximum depth of the chosen depth range (depth ranges are listed in Table 1). The SML is excluded as internal waves cannot exist in homogeneous layers without stratification. To avoid contamination from mixing within frictional boundary layers (a process not included in FS), data within 20 m from the seafloor were excluded from analyses.

- Staircases: Hydrographic profiles were scanned visually for thermohaline staircases. Only for drifts 1 and 3 of the MOSAiC expedition (both in the high Arctic, see Figure 1) were there widely spread double-diffusive staircases. Using a simple algorithm for detecting staircases (effectively defined as large differences between the observed density to the density profile smoothed over a 15-m scale), we then identify the longest continuous segment without a staircase within a predefined depth range. This segment is then used for FS analysis.
- Weak stratification: Segment-average stratification of $\overline{N} < 1 \times 10^{-3}$ rad s$^{-1}$ was deemed below the resolution of density observations and the associated profiles were excluded from the FS analysis as they may lead to erroneous results in the calculation of strain (Equation 1). In the present data set, this only affected four data points of KH Feb 2021.
- Fast Fourier Transform (FFT) lengths: The FFT length for the calculation of shear spectra was limited by the vertical resolution and span of the velocity profiles, and was generally either 16 or 32 points (for computational reasons, powers of two are best suited for FFT). Strain spectra, on the other hand, could be calculated with much longer FFTs (64–256 points) due to their higher vertical resolution. Their length was chosen to match the largest wavelength resolved by the shear spectra.
- Spectral corrections: Vertical (bin-) averaging and first-differencing in data processing introduces spectral attenuation in the high wavenumber end of the shear and strain spectra. The strain spectra were corrected only for first-differencing using the transfer function TF = $\mathrm{sinc}^2(k\Delta_z/(2\pi))$, with the wavenumber vector $k$ and vertical resolution $\Delta_z$ (e.g., Whalen et al., 2015), whereas ADCP processing required correction for vertical smoothing due to range averaging of the pulses using the transfer function TF = $\mathrm{sinc}^2(k\Delta_{pulse}/(2\pi)) * \mathrm{sinc}^2(k\Delta_{bin}/(2\pi))$, with the pulse length $\Delta_{pulse}$ and bin size $\Delta_{bin}$ (Polzin et al., 2002). We note that in this case it was not necessary to correct for first-differencing, as shear spectra were obtained directly from velocity spectra.
- Cutoff wavenumber for integration of spectra: Since hydrographic profiles are taken with high precision and vertical resolution of 0.5–2 m, they generally do not pose a limitation in terms of calculating fine-scale variance. Profiles of velocity (and hence shear) on the other hand, suffer not only from coarser vertical resolution (typically 4–8 m), but also higher susceptibility to noise. For consistency, we use the same wavenumber cutoff for integration to obtain the strain and shear variances. The cutoff was chosen manually for each cruise by visually determining at which wavenumber the (averaged) shear spectrum approaches the shape of noise, increasing as $k^2$ (dashed line Figure 4a). For most cruises, this cutoff was set to vertical wavelengths of 25 m or 30 m, except for two cruises (HM Aug 2015 and HM Sep 2014) with noisier SADCP quality, requiring cutoff wavelength of 50 m.

  For an individual spectrum, the shear variance (i.e., the integral of the shear spectrum up to the cutoff wavenumber) normalized by $N^2$ may exceed the canonical value of 0.66 (in GM76 [see Section 2.5], this is the cutoff value after which dissipation of energy occurs; it is analogous to a critical Froude number). In these so-called "saturated" cases, we find a new, smaller cutoff wavenumber, so that the integral does not exceed 0.66 and recalculate shear and strain variances accordingly. While this is technically correct, it may also introduce biases to the final result of FS due to insufficient bandwidth (Polzin et al., 2014).
- Averaging over casts within a cluster: Within each cluster of casts, the individual spectra (one shear and one strain spectra per cast) are averaged and FS is calculated from the averaged spectra.

### 2.5. Finescale Parameterization (FS)

In this study, we use the FS formulation following Polzin et al. (1995) based on Gregg (1989) where the internal wave energy content is approximated using the shear variance. We adopt the notation as in Fine et al. (2021):

$$\varepsilon = \varepsilon_0 \frac{\overline{N^2}}{N_0^2} \frac{\langle U_z^2 \rangle^2}{\langle U_{zGM}^2 \rangle^2} h_1(R_\omega) L(f, N) \tag{3}$$

with $\varepsilon_0 = 6.73 \times 10^{-10}$ W kg$^{-1}$ and $N_0 = 5.2 \times 10^{-3}$ rad s$^{-1}$, the reference GM values. $\overline{N^2}$ is the segment-averaged Brunt-Väisälä frequency squared, $\langle U_z^2 \rangle$ is the observed average shear variance over the analysis bandwidth (limited by the cutoff wavenumber in the high end) and $\langle U_{zGM}^2 \rangle$ is the same for the GM76 model. The GM model of internal

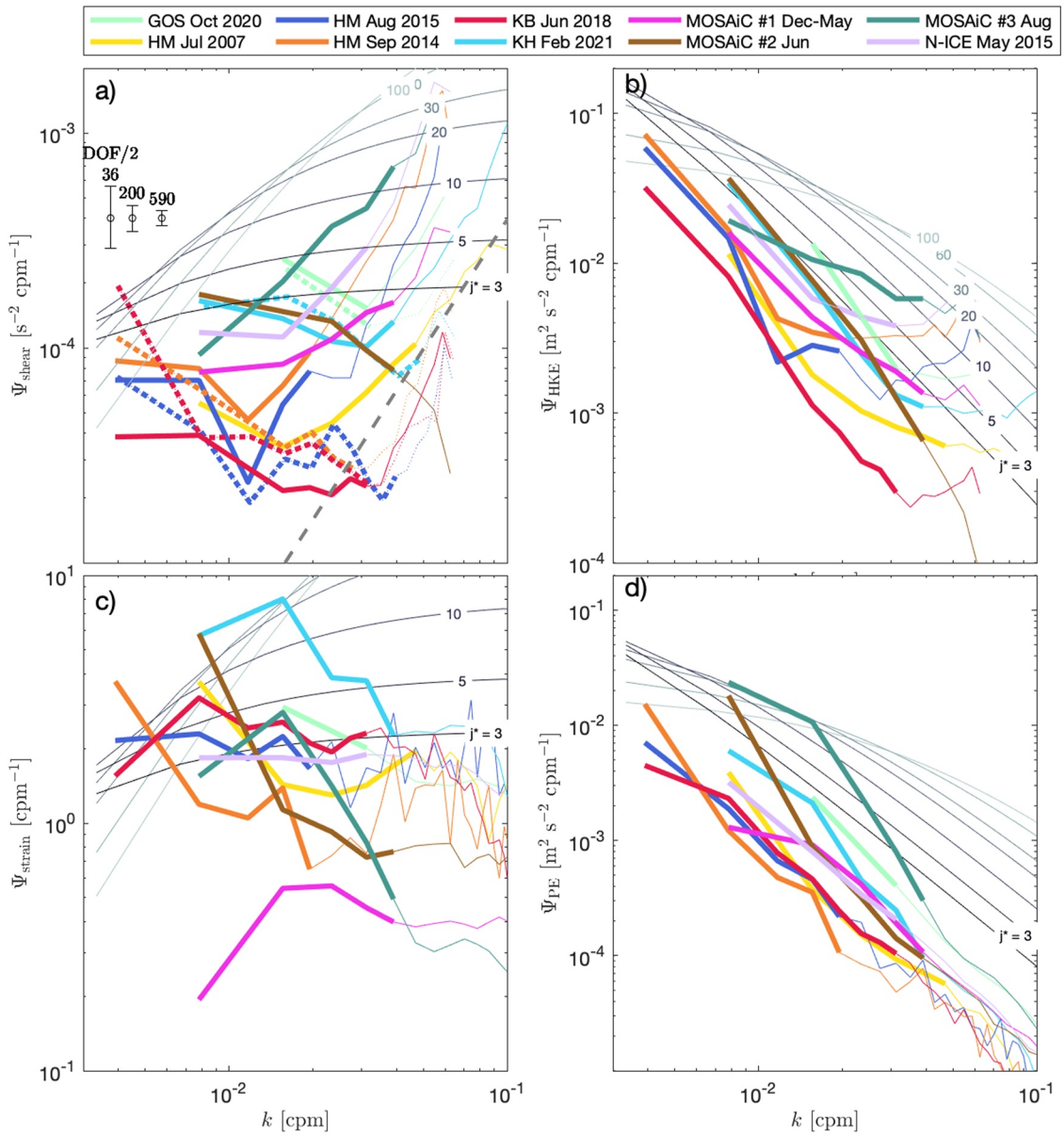


**Figure 4.** Cruise-averaged vertical wavenumber spectra of shear (a), horizontal kinetic energy (HKE, b), strain (c) and available potential energy (PE, d). Dotted lines in the shear spectrum are from lowered acoustic Doppler current profilers (LADCPs), while solid lines stem from ship-mounted acoustic Doppler current profilers (SADCPs). Thick lines indicate parts of the spectra taken into account for Finescale Parameterization (i.e., those parts below the high-wavenumber cutoff chosen for each cruise). Error bars in a) show the 95% confidence interval for the least and most degrees of freedom (DOF, defined as 2× the number of spectra used for averaging; the number of spectra matches the number of microstructure casts in Table 1) as well as for the (rounded) average value of all cruises (200 spectra). Thin gray shaded lines show the GM spectra for various values of $j^*$ and the thick dashed gray line in a) indicates the shape of white noise for the shear spectra (i.e., if observed spectra are parallel to this line, they represent noise).

waves was developed by Garrett and Munk (1972 and 1975) and advanced by Cairns and Williams (1976) to the version "GM76." Here we use the GM76 formulation as provided in the appendix of Gregg and Kunze (1991).

$h_1(R_\omega)$ is a scaling factor defined as

$$h_1(R_\omega) = \frac{3(R_\omega + 1)}{2\sqrt{2}R_\omega\sqrt{R_\omega - 1}}, \tag{4}$$

with the ratio between (normalized) shear and strain

$$R_\omega = \frac{\langle U_z^2 \rangle}{\overline{N^2}\langle \zeta_z^2 \rangle}. \tag{5}$$

$R_\omega$ is the ratio of horizontal kinetic and potential energy (PE), and for a single wave, it can be related to the aspect ratio of the internal wave. For a GM field, $R_\omega = 3$. Finally,

$$L(f, N) = \frac{f \cosh^{-1}\left(\frac{\overline{N}}{f}\right)}{f_{30} \cosh^{-1}\left(\frac{N_0}{f_{30}}\right)} \tag{6}$$

represents a simple correction of the internal wave field for latitude relative to 30° (Gregg et al., 2003).

The FS formulation can equivalently be expressed referencing observed strain instead of shear (e.g., Kunze et al., 2006), yielding

$$\varepsilon = \varepsilon_0 \frac{\overline{N^2}}{N_0^2} \frac{\langle \zeta_z^2 \rangle^2}{\langle \zeta_{zGM}^2 \rangle^2} h_2(R_\omega) L(f, N) \tag{7}$$

with

$$h_2(R_\omega) = \frac{R_\omega(R_\omega + 1)}{6\sqrt{2}\sqrt{R_\omega - 1}}. \tag{8}$$

With a reasonably chosen constant $R_\omega$, this formulation allows for FS estimates of $\varepsilon$ solely based on strain (and thus standard hydrographic profiles) without requiring any observations of velocity shear. Applications of this formulation include global estimates of dissipation rates from the ARGO buoy fleet (Whalen et al., 2015), ice-tethered profilers in the central Arctic (Dosser et al., 2021), and CTD profiles in Canadian Arctic Shelf waters (Chanona et al., 2018). Fine and Cole (2022) point to a significant caveat of this approach: While shear variance can explain 55% of their observed variability of $R_\omega$, strain variance only accounts for 10%, making the FS predictions highly dependent on the choice of $R_\omega$. In this study, we calculate the "strain-only" version of FS to validate it against the "full" (shear & strain) FS and direct observations of dissipation rate. Both "full" and "strain-only" versions of FS yield one estimate of $\varepsilon$ to one set of shear and/or strain spectra over vertical scales of 120–380 m. This estimate is compared to the directly observed $\varepsilon$ values geometrically averaged over the same depth range. In a recent study, Whalen (2021) emphasized the need to average over similar spatio-temporal scales when comparing dissipation measurements with FS estimates. By first vertically averaging, then time averaging over clusters of 10–15 microstructure profiles, each dissipation estimate from both methods involves some spatio-temporal averaging over typical scales of 5–10 hr and several kilometers for each data point presented.

## 3. Results

### 3.1. Internal Wave Field Properties

Average spectra of shear and strain provide a useful insight into the internal wave climate. We analyze their properties in terms of energy, relative amplitude ($R_\omega$) and shape ($j*$, slope). Spectra of horizontal kinetic energy (HKE) and available PE are related to spectra of shear and strain as $\Psi_{HKE} = \Psi_{shear}/(2\pi k)^2/2$ and $\Psi_{PE} = N^2\Psi_{strain}/(2\pi k)^2/2$, respectively. As expected for a somewhat less energetic internal wave environment, cruise-average spectra have generally lower amplitudes compared to GM (Figure 4). However, there is great variability between cruises. Particularly low values of both HKE and PE were recorded during summer north (-west) of Svalbard (HM Aug 2015, HM Sep 2014 and KB Jun 2018). Most energetic in terms of HKE are the records from the Barents Sea (GOS Oct 2020 and KH Feb 2021) and those from the MOSAiC and N-ICE campaigns. However, as we present below, the shape of the spectra of the latter indicate that comparison to traditional GM values might be misleading.

The shear-strain ratio $R_\omega$ is a measure of the aspect ratio of internal waves. For a single wave frequency, $\omega$, it can also be expressed as $R_\omega = \frac{\omega^2 + f^2}{\omega^2 - f^2}$, where $f$ is the local Coriolis parameter. $R_\omega$ is greatest for wave frequencies $\omega$ approaching $f$ and close to unity for $\omega$ approaching $N$ (c.f. Chinn et al., 2016, their Figure 2). For typical

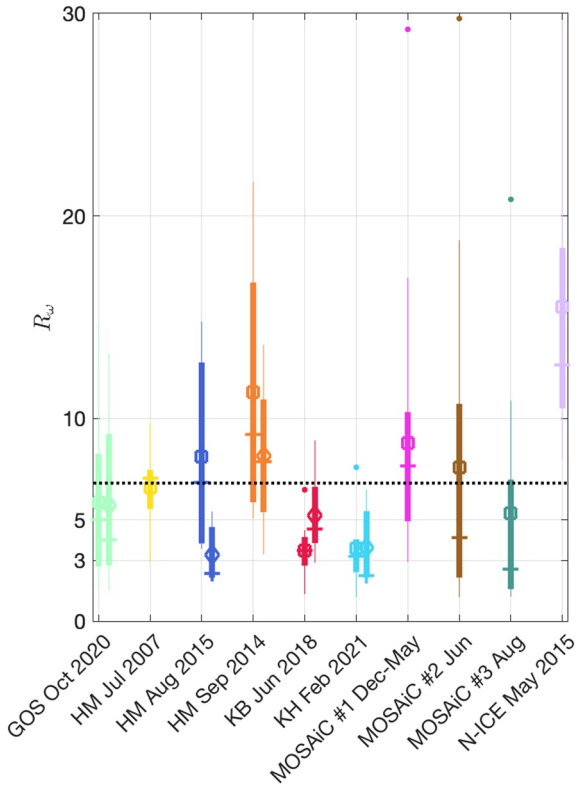


**Figure 5.** Values of $R_\omega$ calculated for each Finescale Parameterization data point as box plots (thick lines mark the interquartile range, thin lines comprise ~99.3% of data, dots are outliers and horizontal bars mark the median). For cruises where lowered acoustic Doppler current profilers profiles are available, a second box is shown with the same color code. Squares show the arithmetic mean for ship-mounted acoustic Doppler current profiler-based estimates, diamonds the arithmetic mean for LADCP-based estimates where available. The over-all average of the means (i.e., of the squares and diamonds) is $R_\omega = 7.2$. The average interquartile range is 5.2 (not shown).

NIWs in the Arctic, for example, using $\omega = 1.02f$ (Alford & Gregg, 2001), $R_\omega \approx 50$. Observed values of $R_\omega$, calculated for each available data point, exhibit great variability (Figure 5), with $R_\omega$ spanning more than one order of magnitude and maxima exceeding 60. The temporal and spatial variability is large, with no apparent geographical or seasonal pattern in the distribution of $R_\omega$. For example, by far the highest values are observed for the N-ICE May 2015 campaign. The same geographical area (Yermak Plateau) is covered by several other cruises (e.g., HM Aug 2015, KB Jun 2018 and, to a certain extent, MOSAiC #2 Jun), each exhibiting substantially lower average values of $R_\omega$. Calculating $R_\omega$ using shear from relatively less noisy LADCP data results in nearly identical (KH Feb 2021 and GOS Oct 2020), somewhat higher (KB Jun 2018) or somewhat lower (HM Aug 2015, HM Sep 2014) values compared to the calculations using the SADCP, suggesting that the range of variability we observe is not due to systematic instrument biases. The cruise-mean values average to about $R_\omega = 7$ (with an average interquartile range of about 5), which we take to be the representative value for average eastern Arctic conditions.

An important element considering the applicability of the GM model to Arctic internal waves is the shape of the spectra. The shape of GM wavenumber spectra in their analytical form depends on three parameters: the bandwidth parameter $j^*$ and the slope parameters $s$ and $r$ (e.g., Eden et al., 2019). For GM76, $r = s$ and the canonical values are $j* = 3$ and $s = 2$. In numerical simulations of energy transfer within internal-wave spectra, Eden et al. (2019) find the energy transfer to be dependent on the spectral slope $s$ and suggest a correction of $\varepsilon_{FS}$ by a factor of $(1 - s)^{-3}$. From global Argo float data, Pollmann (2020) find the slope parameter $s$ (in the strain spectra) to increase with increasing latitude, reaching values of $s \approx 2.5$ in the North Atlantic, which would lead to a correction factor of 0.3 for $\varepsilon_{FS}$. Several of the strain spectra in our observations decrease with increased wavenumbers, consistent with higher-than-GM values for the slope parameter $s$ (Figure 4). However, additionally to $s$, $j^*$ must be considered in the discussion of spectral shape distortions. Unfortunately, the correction for varying s proposed by Pollmann (2020) is not applicable for $j^*$ (i.e., the energy transfer for GM spectra with non-canonical $j^*$ is not known). As discussed in Section 4.1, it is not possible to quantify the contribution of either parameter to the observed spectral distortion using fitting techniques when both distort the spectra in similar ways. The parameter $j^*$ corresponds to the reference vertical mode number, which may also be interpreted as the bandwidth of frequencies taken into account for the model and is canonically set to 3. Previous observations from the Arctic Internal Wave Experiment suggest that some Arctic spectra may be better represented by higher values of $j^* = 20$–$60$ (D'Asaro & Morehead, 1991). In Figure 4 we present a family of curves of GM spectra calculated using $j^*$ values ranging from 3 to 100. We note that strain spectra generally exhibit flatter (or even negative) curves, generally more similar to GM76 with low $j^*$ values around the canonical value of 3 (Figure 4c). Cruise-averaged shear spectra, on the other hand, appear to be better represented by high $j^*$ values, over at least part of the wavenumber range (e.g., MOSAiC #3 Aug, MOSAiC #1 Dec–May, HM Jul 2007, N-ICE May 2015 and HM Sep 2014). The same is true for HKE spectra. The somewhat surprising high HKE in the MOSAiC #1 & #3 and N-ICE spectra may be explained such that their shape might best be compared to GM spectra with greater $j^*$ values, which also exhibit substantially greater energy in the relevant wavenumber range (Figure 4b). It is evident from Figure 4 that no single $j^*$ value represents the shape of all the observed cruise-average spectra. The physical interpretation of these results is not straightforward, but they are suggestive of an internal wave field whose properties partly differ from GM. High values of $R_\omega$ are indicative of a prevalence of NIWs (Ijichi & Hibiya, 2015), whose energy is comparable to GM, but distributed over spectra with differing slopes and/or many more vertical modes (i.e., $j^* > 3$). The effect of these deviations from GM on the theoretical underpinnings of the FS is difficult to assess, but errors or biases may be expected (c.f. Polzin et al., 2014; Takahashi & Hibiya, 2021).

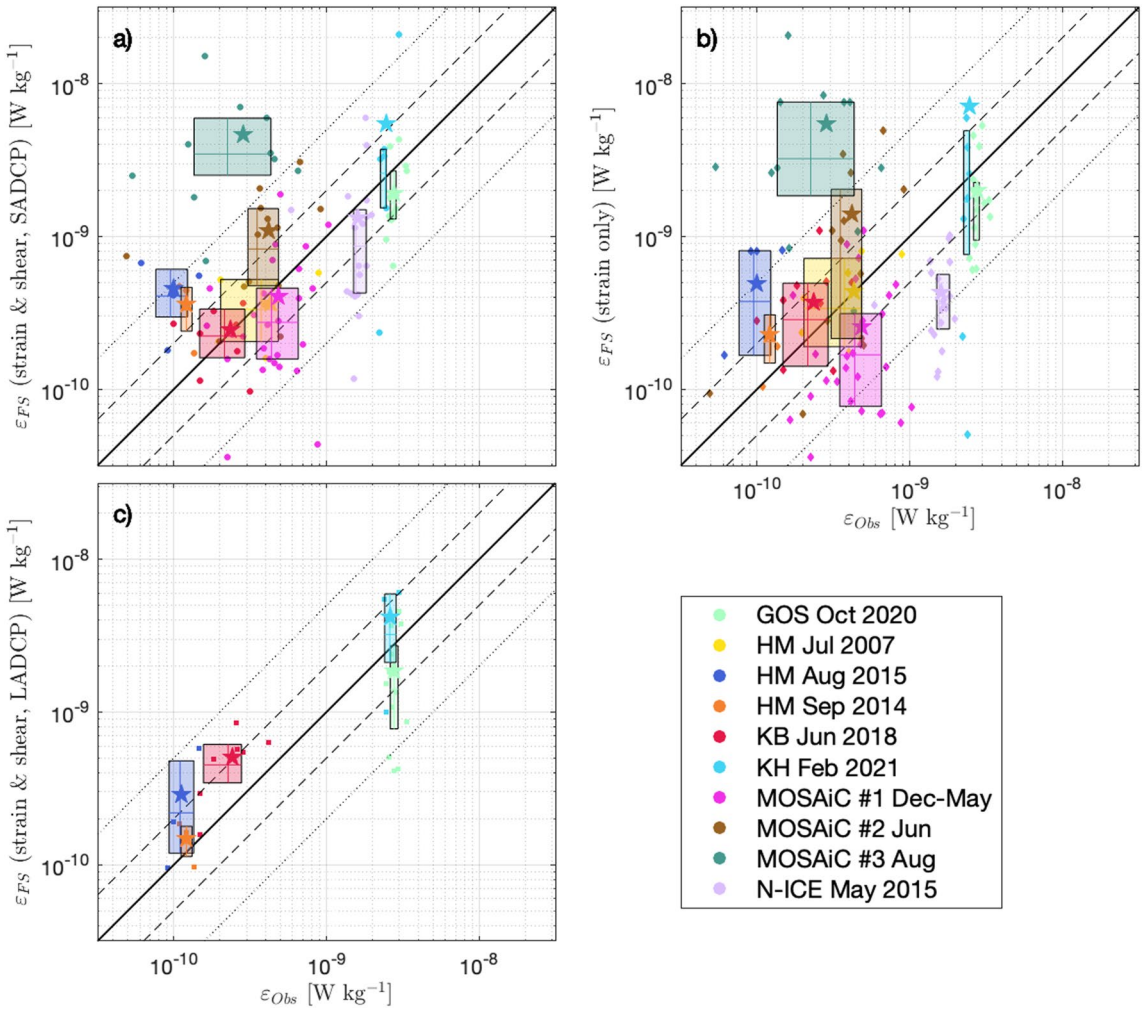


**Figure 6.** Scatters of dissipation rate ($\varepsilon$) derived from finescale parameterization (FS) using (a) strain and shear from ship-mounted acoustic Doppler current profiler, (b) strain only and (c) strain and shear from lowered acoustic Doppler current profilers, plotted against observations. Boxes indicate the interquartile range between the 25th and 75th percentile. Lines within the boxes show the geometric mean. Stars show the arithmetic mean of the scatters. Solid, dashed and dotted lines indicate factors of 1, 2, and 5 agreement between directly observed and FS values, respectively.

### 3.2. FS Compared With Direct Observations of $\varepsilon$

The results of the full FS (computed using both shear and strain, with the shear obtained from SADCPs) are compared to direct observations in Figure 6a. Geometric means of $\varepsilon_{FS}$ of all cruises apart from MOSAiC #3 are within a factor of 5 from direct observations and six of them are within a factor of two, which may be considered an excellent agreement. The arithmetic mean (stars) exceeds the geometric mean for each cruise due to the great impact of outliers on logarithmic scales. The variability of the estimates for each cruise can be considerable (see boxes in Figure 6, that represent the interquartile range between the 25th and 75th percentile). A useful metric of variability is the factor of $\varepsilon$ spanned by the interquartile range (i.e., $\varepsilon_{75^{th}}/\varepsilon_{25^{th}}$). A larger factor indicates a larger variability. The variability for the full FS estimates using SADCP, averages to a factor of 2.5 over all cruises and varies between 1.9 for HM Sep 2014 and 3.5 for N-ICE. For the direct observations, average interquartile range is within a factor of 1.7, varying between 1.1 for GOS Oct 2020 and 3.2 for MOSAiC #3. Apart from MOSAiC #3, the interquartile range is always greater for FS estimates than for observations.

Lowered ADCPs were available for five cruises. Comparing FS based on LADCP data (Figure 6b) to FS based on SADCP data (Figure 6a), we find that in terms of geometric averages, the performance of FS based on LADCP data is substantially better for HM Aug 2015 and HM Sep 2014 and slightly worse for the other cruises. Nevertheless, the geometric averages of all cruises are within a factor of 2 compared to direct observations (Figure 6b).

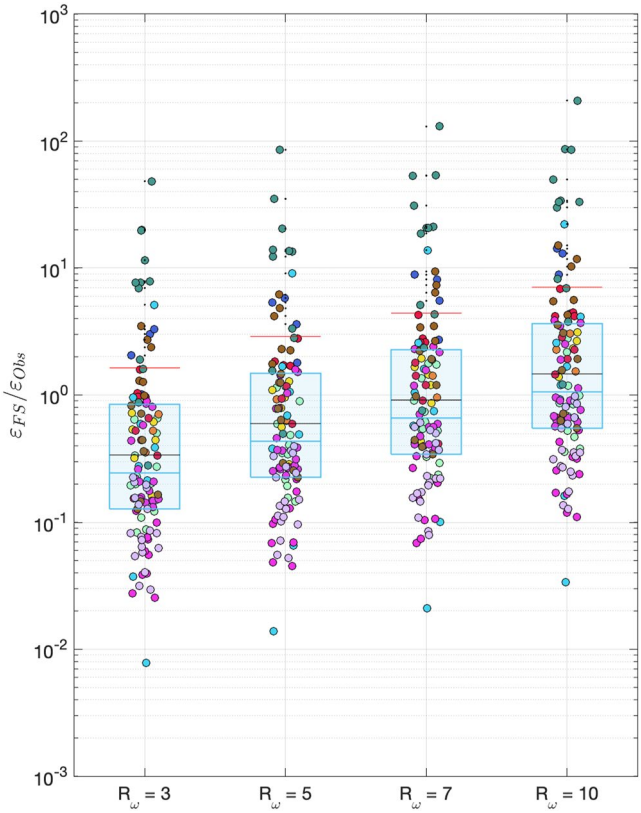


**Figure 7.** Performance of strain-based Finescale Parameterization for various values of $R_\omega$. Dots are color coded per cruise as in previous figures. The offset of the dots from the center line ("jitter") is introduced randomly to increase readability. Boxes indicate interquartile range with the median indicated as blue line. The geometric mean is shown as black line, whereas the arithmetic mean is presented as red line.

The variability of FS estimates within each cruise is similar as before, with the FS interquartile range averaging 2.7.

Using a value of $R_\omega$ fixed to 7 (corresponding approximately to the average cruise-mean value of observed $R_\omega$; see Figure 5), the strain-only formulation of FS performs reasonably well. Despite the very large range of observed $R_\omega$ (Figure 5), almost all estimates of cruise-averaged $\varepsilon$ are within a factor of 5 of the directly observed values. In terms of variability, the strain-only formulation results in more spread of estimated $\varepsilon$ compared to the full FS, with interquartile ranges averaging 4.3, reaching a maximum of 9.5 for MOSAiC #2.

Using a factor of 2 between FS and observations as benchmark for excellence, 47% of clusters satisfy this criterion for full FS. A higher percentage of excellent agreement is obtained using the full FS and LADCP, with 55%. For the strain-only FS, the average drops to 34%. A similar tendency also holds for larger thresholds: A factor of 5 may constitute acceptable agreement and is achieved for 84%, 90%, and 73% of data points using full FS, full FS with LADCP and strain-only FS, respectively.

### 3.3. Internal Wave Field Properties Impacting FS Performance

The choice of the shear-to-strain ratio R$_\omega$ when using the strain-only formulation of FS has direct and substantial effect on the performance of FS. Using the canonical value of 3 would lead to a systematic underestimation of $\varepsilon$ by a factor of 3 in the Eastern Arctic environment (Figure 7). Although the variability of strain-only FS performance is high (the interquartile range spans a factor of 6.5), this offset is substantial. We note that arithmetic averages of all clusters is biased significantly high due to the outliers (mainly from MOSAiC #3). The environmental impacts on the performance of full FS are more nuanced. When both shear and strain observations are available, even highly variable and non-GM-like R$_\omega$ values as observed here (Figure 5) do not systematically impact the performance of FS (Figure 8g). The bandwidth of internal waves is bounded by the Coriolis parameter $f$ and the Brunt-Väisälä frequency $N$. Using canonical GM values ($N = 5.24 \times 10^{-3}$ s$^{-1}$ and $f_{30} = 7.292 \times 10^{-5}$ s$^{-1}$) yields a bandwidth ($N/f$) of 72. In high latitudes $f$ is much greater ($f_{80} = 1.436 \times 10^{-4}$ s$^{-1}$), thus there is a tendency to reduce the bandwidth of the internal wave spectrum. However, this can be (partially) compensated by increasing stratification. Our observations showed a wide range of profile-average stratification, averaging to $N = 4 \times 10^{-3}$ s$^{-1}$ in a range from $N = 4.8 \times 10^{-4}$ s$^{-1}$ to $N = 1.1 \times 10^{-1}$ s$^{-1}$. This means that while for some profiles, increased $N$ compensated for increased $f$ to maintain a bandwidth similar to GM, most of the profiles were taken in internal wave climates with much narrower bandwidth (Figure 8b). Although the change of bandwidth is addressed by the term $L(f, N)$ in Equation 3 and for most clusters, we do not observe any notable dependence of FS performance on the bandwidth (Figure 8b), the poor performance of MOSAiC #3 coincides with large bandwidth (>50) despite its high-Arctic location (see Figure 1). Accordingly, MOSAiC#3 stands out with its exceptionally strong stratification (Figure 8a).

To assess the more subtle influence of other environmental parameters (the relatively wide spread of data renders simple regression analysis inconclusive), we focus on the outliers of FS performance (i.e., those values that over- or underestimate $\varepsilon$ by more than a factor of 5) and in how far they are subject to common environmental properties. Shear variance is a fundamental property of the internal wave field. In our analysis there is a tendency for large shear variances to be associated with an overestimation of FS (high-outliers in Figure 8c average to $1.2 \times 10^{-5}$). Conversely, the clusters for which FS underestimates $\varepsilon$ tend to have smaller shear variances (on average $2.3 \times 10^{-6}$). Interestingly, such a pattern is not apparent for the strain variance (Figure 8d). The picture becomes more clear, when considering the parameters HKE and PE. Both show a pronounced tendency for high-outliers to be situated in high energy environments ($3.9 \times 10^{-4}$ and $2.9 \times 10^{-4}$ m$^2$ s$^{-2}$, for HKE and PE, respectively) as opposed to low-outliers ($7.2 \times 10^{-5}$ and $1.2 \times 10^{-5}$ m$^2$ s$^{-2}$). Finally, we also note that while FS performs very well in highly turbulent environments, there is a tendency to overestimate $\varepsilon$ in low-turbulence

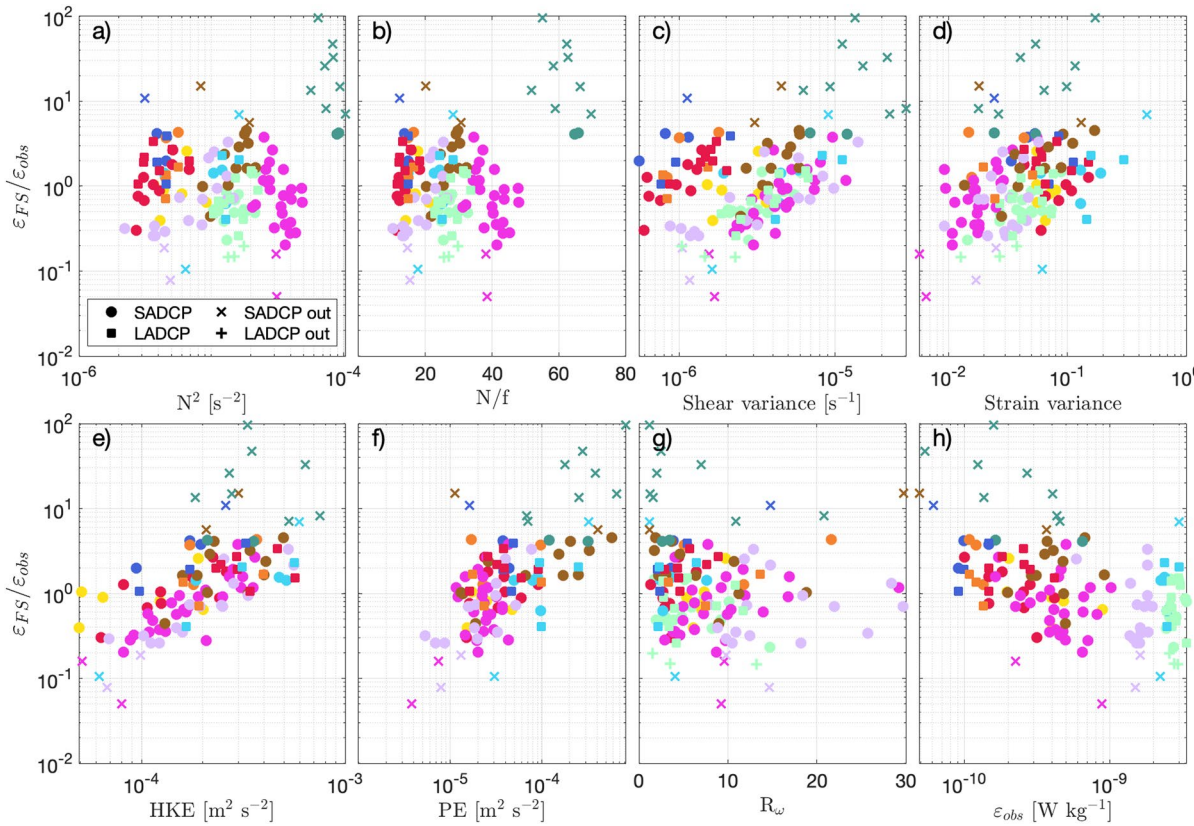


**Figure 8.** Ratio of Finescale Parameterization (FS)-derived to directly-observed dissipation rate ($\varepsilon_{FS}/\varepsilon_{obs}$) plotted as function of parameters quantifying the state of the background internal wave field. Color coding is by cruise as before. Dots indicate SADCP-derived FS, squares are LADCP-derived FS. "x" and "+" markers indicate datapoints outside a factor of 5 between $\varepsilon_{FS}$ and $\varepsilon_{obs}$ for ship-mounted acoustic Doppler current profiler and lowered acoustic Doppler current profilers derived FS, respectively.

environments (high-outliers have a geometric mean of $2.2 \times 10^{-10}$ W kg$^{-1}$, compared to $1.5 \times 10^{-9}$ W kg$^{-1}$ for low-outliers (Figure 8h)).

## 4. Discussion

Microstructure-based estimates of dissipation rate and FS-based estimates are obtained from measurements at different spatio-temporal scales and should be averaged accordingly (Whalen, 2021). Thus, comparison of the two methods is most meaningful when averaged over several casts, as in the clusters we use. We assume that FS-derived $\varepsilon$ estimates represent typical values of $\varepsilon$, which are represented by the geometric averages of the assumed (near-) log-normal distributions. We note however, that the net dissipation in the ocean would be controlled by the contribution of a small number of high-end outliers. Consequently, if indeed FS estimates characterize typical values, then we do expect them to underestimate the net dissipation. Apart from the high bias of MOSAiC#3, the overall performance of FS fulfills the expectation expressed by Polzin et al. (2014), that "the biases associated with results of carefully implemented finescale parameterizations should be substantially less than an order of magnitude over much of the ocean." However, the performance with respect to individual clusters appears to be substantially worse than for other regions of the world ocean: For example, for the strain-only FS, only 34% of FS estimates fall within a factor of 2 of direct observations; whereas this was true for 81% of FS estimates obtained from Argo data in 7 regions around the mid-latitude world ocean (Whalen et al., 2015).

### 4.1. The Eastern Arctic Internal Wave Field and FS Performance

FS is defined by scaling observed properties of the internal wave field against those described in GM. For this method to work, both internal wave fields should be comparable in terms of spectral shapes. Unfortunately, there are no clearly defined criteria that could serve as a measure for the applicability of the method.

Kinetic and potential energies of the internal wave field observed here are generally lower but within an order of magnitude of the GM, and are thus somewhat more energetic than most previously reported records from various regions in the Arctic (e.g., Levine et al., 1987; Padman & Dillon, 1989; D'Asaro & Morehead, 1991; Fine et al., 2021). This is likely due to prevalence of data from the comparably shallow and dynamic Barents Sea and the Yermak Plateau, which are influenced by rough topography and substantial tidal currents. We note, however that some of the most energetic PE and HKE spectra stem from MOSAiC #3 and were obtained during summer in the central Arctic Ocean.

In terms of spectral shape, both the slope parameter $s$ and the bandwidth parameter $j^*$ control the shape of GM spectra. For environments where observed spectra have slopes differing from canonical GM ($s = 2$), Eden et al. (2019) introduced a correction factor to FS, compensating for changing energy content of these observed spectra. In an high-latitude Southern Ocean application, Takahashi and Hibiya (2021) observed shear and strain spectra that were distorted compared to GM and found that the correction factor introduced by Eden et al. (2019) improved their FS results. However, this correction assumes that spectra deviating from GM76 still maintain the canonical GM76 equality $r = s$ for the two slope parameters in the general formulation of GM (Eden et al., 2019). In an Arctic context, we expect $j^*$ to vary and distort the spectrum as well (D'Asaro & Morehead, 1991; Fer et al., 2010). In this work, we note that spectra of shear and HKE are generally more similar to GM with values of $j^*$ greater than the canonical $j^* = 3$ (Figures 4a and 4b). This is largely consistent with previous findings: for example, D'Asaro and Morehead (1991) obtained best fit (to GM75) values of $j^*$ between 20 and 60 for the high and low wavenumber part of their observed Arctic velocity spectra, respectively. Large values of $j^*$ indicate that the Arctic internal wave field tends to support a higher number of modes than the mid-latitude Ocean. Neither changes of $s$ nor of $j^*$ conserve energy and GM spectra with greater $j^*$ or $s$ are more energetic over the relevant wavenumber range, potentially leading FS to overestimate $\varepsilon$. While there exists a correction for varying $s$, this is not the case for $j^*$ (i.e., the energy transfer for GM spectra with non-canonical $j^*$ is not known). And with both parameters expected to vary and distorting the spectra in similar ways, it is in this case not possible to quantify the contribution of either parameter to the observed spectral distortion using fitting techniques (as used in Pollmann, 2020). Using eikonal calculation, Takahashi et al. (2021) investigate the effect of "humps" in observed spectra on FS. The spectral humps are regions of elevated amplitude in the low wavenumber part of the spectra (i.e., those that are used for FS) and are indicative of the prevalence of NIWs and/or bottom-generated lee waves in the spectra. The authors find these humps to cause FS to overestimate $\varepsilon$. Several of our cruise-averaged shear and strain spectra show hump-like features (e.g., KH Feb 2021, HM Aug 2015 or KB Jun 2018, Figure 4), however these do not appear to systematically overestimate FS in our analysis (cf. Figure 6). Ultimately, we conclude that applying FS to spectra whose shape deviates substantially from GM may be ill-advised.

The shear-strain ratio $R_\omega$ and its variability have been explicitly discussed by Chinn et al. (2016) in the Pacific and Fine et al. (2021) in the (western) Arctic: Using data from 14 moorings in the Pacific Ocean, Chinn et al. (2016) found time-average values of $R_\omega$ between 1 and 10, but changes of the order 10 were observed on all temporal scales from days to months. In an Arctic setting, using an 8-day long moored time series in the Beaufort Sea (~3,500 m bottom depth), Fine et al. (2021) found highly variable $R_\omega$ averaging to a value of 17, in a range from 3 to 50. In agreement with Chinn et al. (2016), they attribute the variability and magnitude of $R_\omega$ to the strong near-inertial component of the internal wave field. Our observed $R_\omega$ from 8 different cruises across the Atlantic sector of the Arctic Ocean range between 1 and 30 (with an average interquartile range of 5.2) and are comparable in terms of variability to the findings of Fine et al. (2021), but average to lower value of ~7, which corresponds to the global average value reported by Kunze et al. (2006) (Figure 5).

The variability of $R_\omega$ itself does not appear to systematically bias the full FS (Figure 8e), indicating that the term $h_1(R_\omega)$ in Equation 3 performs as desired in Arctic conditions. However, when using a fixed $R_\omega$ to perform the strain-only (or, in fact, the rarely used but theoretically possible shear-only) form of FS, the difference between assumed and real $R_\omega$ can produce strong biases (Chinn et al., 2016; Fine et al., 2021). This uncertainty of $R_\omega$ is likely the reason for the generally higher spread and high standard deviations in the strain-only FS (Figure 6b). We advise caution when using this method, especially when only few data points are available. We do note however, that $R_\omega = 7$ appears to be a reasonable choice for the whole domain as there is no systematic over- or under-estimation of $\varepsilon_{FS}$ compared to direct observations.

### 4.2. The Case of MOSAiC #3

MOSAiC #3 is unique because of the great overestimation of $\varepsilon$ in FS compared to observations (by a factor of 15 on the geometric average, see Figure 6). This is the case for full FS as well as for strain-only FS, however,

the offset of the strain-only formulation may be reduced somewhat by using a smaller value of $R_\omega$; Figure 5 suggests that a value between 3 and 5 would be more appropriate for the summertime high-Arctic environment of MOSAiC #3. In terms of spectral properties, shear and HKE are clearly similar to GM with very high $j^* = 60$–$100$ (Figure 4). In fact, the shear spectra of MOSAiC #3 are unique in that they are consistently parallel to high $j^*$ GM throughout the wavenumber range; that is, even at the most robustly resolved smallest wavenumbers. The cruise-average strain spectrum associated to MOSAiC #3, does not stand out, but the average PE spectrum is remarkable in that it is the most energetic (largely even surpassing GM with $j^* = 3$) throughout the wavenumber range (Figure 4). This is due to the exceptionally high stratification associated to these observations (Figure 8a). As there appears to be a dependence of FS performance on energy levels, as well as on directly observed dissipation rate (Figures 8e, 8f, and 8h), the combination of relatively high HKE and exceptionally high PE during MOSAiC #3 in a low-turbulence environment may result in particularly non-GM-like conditions, causing FS to dramatically overestimate directly observed dissipation rates.

### 4.3. Alternative Formulations of GM

A shelf-specific version of FS has been developed by MacKinnon and Gregg (2003) and accounts for the coastal internal wave field in which low and high modes are disconnected and thus large- and small-scale waves may not maintain the steady energy cascade by wave-wave interactions needed for the classical FS. The distribution of $\varepsilon$ mapped in $N^2 - Shear^2$-space is a good indicator for applicability of this method (see MacKinnon & Gregg, 2003, their Figure 13). From our relatively limited data in the Barents Sea, $\varepsilon$ mapped in $N^2 - Shear^2$-space does not appear to follow the pattern expected from the MacKinnon and Gregg (2003) parameterization (not shown). However, Sundfjord et al. (2007) reported favorable comparison with the MacKinnon and Gregg (2003) formulation for their data in the marginal ice zone of the Barents Sea. In this formulation, $\varepsilon$ is obtained by

$$\varepsilon_{MG} = \varepsilon_0 \left(\frac{N}{N_0}\right)\left(\frac{S_{lf}}{S_0}\right) \tag{9}$$

with $\varepsilon_0$ taken to be the cruise-average $\varepsilon$, $S_{lf}$ the (6-hr) low-pass filtered shear and $N_0 = S_0 = 3$ cph, the reference values for buoyancy and shear, set to 3 for simplicity. We find that the shelf-specific FS does capture the variability of directly observed $\varepsilon$ quite well, actually producing less spread than the more complete formulations of FS used in this study. Remarkably this is true for the whole data set, independent of actual bottom depth. This implies that vertically averaged values of shear and $N$ are generally good indicators for $\varepsilon$ variability. However, the amplitude of $\varepsilon_{MG}$ strongly depends on the value of $\varepsilon_0$, thus severely limiting its usefulness in assessing $\varepsilon$ without prior knowledge.

Ijichi and Hibiya (2015) devised a correction for FS for internal wave climates dominated by NIWs (i.e., $R_\omega \gg 3$). In their modification, they replace the frequency dependent terms $h_1(R_\omega)$ an $L(f, N)$ in Equation 3 with the following term:

$$h_{mod}(R_\omega, N/f) = \begin{cases} \frac{1+1/R_\omega}{4/3}\frac{L_1}{L_0}R_\omega^{-L_2} & (R_\omega < R_c = 9) \\ \frac{1+1/R_\omega}{4/3}\frac{1}{L_0}\sqrt{\frac{2}{R_\omega - 1}} & (R_\omega > R_c = 9) \end{cases} \tag{10}$$

where $L_0 = 2\pi^{-1}\cosh^{-1}(N_0/f_0)$, $L_1 = 2\mu_{GM}^2$, $L_2 = \log_3(2\mu_{GM})$ and finally $\mu_{GM} = 2\pi^{-1}\cosh^{-1}(N/f)$. This leads to a lower estimate of $\varepsilon_{FS}$ for high $R_\omega$, which Ijichi and Hibiya (2015) found to be a better fit to their data. In our case however, the original FS already performs well (c.f. Figure 6) and the Ijichi & Hibiya modification introduces a low-bias by a factor of around 3 (not shown).

### 4.4. Limitations Due To Noise Floor in Observations

Direct measurements of $\varepsilon$ rely on specialized microstructure instruments with delicate shear probes that require careful deployment procedures and extensive processing. This limits the amount of available data and the result can still be problematic in low-turbulence environments where the dissipation rate is close to the noise level of the instrument (this is true for substantial parts of the data set analyzed here). While great care has been taken to alleviate associated biases in this analysis, these issues limit a straight-forward, widespread comparison of FS and direct observations. A prospective improvement may lie in using fast temperature probes instead of shear probes

to measure $\varepsilon$ in relatively quiescent environments (e.g., Fer et al., 2014; Goto et al., 2021). This removes the need for free-falling instruments, so that the probes may be easily attached to standard CTD-frames, which could lead to a much greater data coverage. Recent tests indicate that temperature-derived measurements of $\varepsilon$ can provide $\varepsilon$ in a range from $10^{-11}$ to $10^{-8}$ W kg$^{-1}$, thus having a significantly lower noise level than shear-based estimates (Yasuda et al., 2021).

The noise floor of the fine-scale observations used in the parameterization also has an effect on the FS estimates. The primary impact is from the noise in the finescale shear that is typically measured by acoustic profilers. Detailed discussion on the limitations of the finescale method is given in Polzin et al. (2014). Assuming a velocity noise of 1 cm s$^{-1}$ in our data and applying it to the calculation of FS, we estimate a lower detection level of $\sim 2–4 \times 10^{-11}$ W kg$^{-1}$ for the FS dissipation rate. This below the dissipation rates we find in our analysis (Figure 6).

## 5. Conclusion

We used observations from 8 Arctic cruises to systematically test the FS in a variety of Arctic conditions. The shear-strain ratio $R_\omega > 3$ suggests that the internal wave field is dominated by NIWs ($R_\omega > 3$), which is a clear deviation from the canonical Garrett & Munk internal wave field. However, we find that FS performs largely satisfactorily in terms of estimating the dissipation rate of turbulent kinetic energy $\varepsilon$ in approximate agreement with direct observations of $\varepsilon$ when averaged on similar spatio-temporal scales. Using the full FS with shear based on SADCP data, 84% of FS-derived values of $\varepsilon$ are within a factor of 5 to observations. For the strain-only version of FS, this percentage was slightly reduced to 73%, indicating that a fixed shear-strain ratio $R_\omega = 7$ is a reasonable choice for a broad range of (eastern) Arctic conditions. Best results were obtained with the full FS and the use of higher-resolution and lower-noise (compared to SADCP) LADCP data, yielding 90% agreement within a factor of 5. Alternative formulations of FS as introduced by Ijichi and Hibiya (2015) and MacKinnon and Gregg (2003) do not appear to provide improvements for general Arctic applications.

One of the goals of this study is to test FS over a wide range of Arctic oceanographic conditions to indentify the conditions that are favorable or detrimental for the application of FS. Notwithstanding the special case of MOSAiC #3, in our data we do not find a conclusive indication that the performance of FS is dependent on the bandwidth of the internal wave field ($N/f$) or the shear-strain ratio $R_\omega$ (Figures 8b and 8g). On the other hand, FS performance appears to be sensitive to HKE and PE, with low (high) energies more often being associated with underestimation (overestimation) of $\varepsilon$ (Figures 8e and 8f). We note that this tendency is more difficult to discern in the variances of shear and strain even though they are closely related to HKE and PE, respectively (Figures 8c and 8d). The generally poor performance of FS for the data set of MOSAiC #3 coincides with outstanding values for a number of environmental parameters: Both shear and HKE spectra are relatively energetic, but differ in their shape substantially from GM (Figure 4). Additionally, the strong stratification and elevated PE in a low-turbulence environment could contribute to the overestimation of FS-derived values of $\varepsilon$ (Figures 8f and 8h).

The outlook of the application of FS in a changing Arctic Ocean is complex. Although the declining sea-ice cover is associated with an increase in near-inertial energy input, this does not currently translate to an observable increase in internal-wave driven turbulence (Fine & Cole, 2022). However, the ongoing "Atlantification" of the eastern Arctic Ocean also leads to a decrease in stratification (Polyakov et al., 2017, 2018). Our results suggest that this environment may be increasingly well suited for the application of FS to monitor mixing and associated vertical fluxes of heat and nutrients that play a key role in changing the eastern Arctic Ocean (Polyakov et al., 2017; Schulz et al., 2022a). On the other hand, observed increases in stratification in the western Arctic Ocean (e.g., Polyakov et al., 2018) may thwart the application of FS. Nevertheless, our results generally show that a careful application of FS can work reasonably well in a wide range of Arctic conditions.

Considering that typical variability of $\varepsilon$ easily exceeds one order of magnitude, the results obtained using applications of FS are likely adequate and allow new insights on the magnitude and distribution of ocean mixing processes and the related water mass transformations. We thus consider FS a powerful tool for the assessment and monitoring of internal-wave-generated mixing and associated heat fluxes in the Arctic Ocean.

## Data Availability Statement

Data sets for GOS Oct 2020 (microstructure: Fer, Baumann, Elliott, & Kolås, 2023; CTD & ADCP: Fer, Skogseth, et al., 2023), KH Feb 2021 (microstructure: Fer, Baumann, Kalhagen, et al., 2023, CTD & ADCP: Fer, Nilsen, Baumann, et al., 2023), HM Aug 2015 (Fer & Kolås, 2018), KB Jun 2018 (Fer, Koenig, Bosse, et al., 2020), and

N-ICE May 2015 (Meyer, Fer, Sundfjord, Peterson, Smedsrud, et al., 2016; Provost et al., 2016) are available with a Creative Commons Attribution 4.0 International License. Data sets from HM Jul 2007 and HM Sep 2014 are under preparation and will be made available at the Norwegian Marine Data Centre. ADCP and MSS data from MOSAiC are openly available (Baumann et al., 2021; Schulz et al., 2022b).

**Acknowledgments**
The work was funded through the AROMA (Arctic Ocean mixing processes and vertical fluxes of energy and matter) project by the Research Council of Norway, Grant 294396. We acknowledge the support of the international Multidisciplinary drifting Observatory for the Study of the Arctic Climate (MOSAiC) project with the tag MOSAiC20192020 and the Project_ID: AWI_PS122_00. A detailed acknowledgment for the expedition can be found in Nixdorf et al. (2021). Financial support for the MOSAiC microstructure data processing was received from the German Federal Ministry for Science and Education (BMBF) and UK Natural Environment Research Council (NERC) funded PEANUTS-project (Grant 03F0804A). Insightful comments from Stephanie Waterman, the editor Takeyoshi Nagai and one anonymous reviewer helped improve the manuscript.

## References

Alford, M. H., & Gregg, M. C. (2001). Near-inertial mixing: Modulation of shear, strain and wave in the Banda Sea at low latitude. *Journal of Geophysical Research*, *106*(C8), 16947–16968. https://doi.org/10.1029/2000jc000370

Baumann, T. M., Fer, I., Bryhni, H., Peterson, A. K., Allerholt, J., Fang, Y.-C., et al. (2021). Under-ice current measurements during MOSAiC from a 75 kHz acoustic Doppler profiler. *PANGAEA*. https://doi.org/10.1594/PANGAEA.934792

Cael, B. B., & Mashayek, A. (2021). Log-skew-normality of ocean turbulence. *Physical Review Letters*, *126*(22), 224502. https://doi.org/10.1103/PhysRevLett.126.224502

Cairns, J. L., & Williams, G. O. (1976). Internal wave observations from a midwater float, 2. *Journal of Geophysical Research*, *81*(12), 1943–1950. https://doi.org/10.1029/jc081i012p01943

Carmack, E., Polyakov, I., Padman, L., Fer, I., Hunke, E., Hutchings, J., et al. (2015). Toward quantifying the increasing role of oceanic heat in sea ice loss in the new Arctic. *Bulletin of the American Meteorological Society*, *96*(12), 2079–2105. https://doi.org/10.1175/BAMS-D-13-00177.1

Chanona, M., & Waterman, S. (2020). Temporal variability of internal wave-driven mixing in two distinct regions of the Arctic Ocean. *Journal of Geophysical Research: Oceans*, *125*(10), 1–23. https://doi.org/10.1029/2020JC016181

Chanona, M., Waterman, S., & Gratton, Y. (2018). Variability of internal wave-driven mixing and stratification in Canadian Arctic shelf and shelf-slope waters. *Journal of Geophysical Research: Oceans*, *123*(12), 9178–9195. https://doi.org/10.1029/2018JC014342

Chinn, B. S., Girton, J. B., & Alford, M. H. (2016). The impact of observed variations in the shear-to-strain ratio of internal waves on inferred turbulent diffusivities. *Journal of Physical Oceanography*, *46*(11), 3299–3320. https://doi.org/10.1175/JPO-D-15-0161.1

D'Asaro, E. A., & Morehead, M. D. (1991). Internal waves and velocity fine structure in the Arctic Ocean. *Journal of Geophysical Research*, *96*(C7), 12725–12738. https://doi.org/10.1029/91jc01071

Dörr, J., Årthun, M., Eldevik, T., & Madonna, E. (2021). Mechanisms of regional winter sea-ice variability in a warming Arctic. *Journal of Climate*, *34*(21), 8635–8653. https://doi.org/10.1175/jcli-d-21-0149.1

Dosser, H. V., Chanona, M., Waterman, S., Shibley, N. C., & Timmermans, M. (2021). Changes in internal wave-driven mixing across the Arctic Ocean: Finescale estimates from an 18-year pan-Arctic record. *Geophysical Research Letters*, *1*(8), 1–10. https://doi.org/10.1029/2020gl091747

Dosser, H. V., & Rainville, L. (2016). Dynamics of the changing near-inertial internal wave field in the Arctic Ocean. *Journal of Physical Oceanography*, *46*(2), 395–415. https://doi.org/10.1175/JPO-D-15-0056.1

Eden, C., Pollmann, F., & Olbers, D. (2019). Numerical evaluation of energy transfers in internal gravity wave spectra of the ocean. *Journal of Physical Oceanography*, *49*(3), 737–749. https://doi.org/10.1175/JPO-D-18-0075.1

Fer, I. (2006). Scaling turbulent dissipation in an Arctic fjord. *Deep-Sea Research Part II: Topical Studies in Oceanography*, *53*(1–2), 77–95. https://doi.org/10.1016/j.dsr2.2006.01.003

Fer, I., Baumann, T. M., Elliott, F., & Kolås, E. (2023). Ocean microstructure measurements using an MSS profiler during the Nansen Legacy cruise, GOS2020113, October 2020. https://doi.org/10.21335/NMDC-239170563

Fer, I., Baumann, T. M., Kalhagen, K., Koenig, Z., & Kolås, E. H. (2023). Ocean microstructure measurements using an MSS profiler during the Nansen Legacy cruise, KH2021702, February 2021. https://doi.org/10.21335/NMDC-1939445412

Fer, I., Bosse, A., Ferron, B., & Bouruet-Aubertot, P. (2018). The dissipation of kinetic energy in the Lofoten Basin Eddy. *Journal of Physical Oceanography*, *48*(6), 1299–1316. https://doi.org/10.1175/JPO-D-17-0244.1

Fer, I., Koenig, Z., Bosse, A., Falck, E., Kolås, E., & Nilsen, F. (2020). Physical oceanography data from the cruise KB 2018616 with R.V. Kristine Bonnevie. https://doi.org/10.21335/NMDC-2047975397

Fer, I., Koenig, Z., Kozlov, I. E., Ostrowski, M., Rippeth, T. P., Padman, L., et al. (2020). Tidally forced lee waves drive turbulent mixing along the Arctic Ocean margins. *Geophysical Research Letters*, *47*(16), 1–10. https://doi.org/10.1029/2020GL088083

Fer, I., & Kolås, E. (2018). Ocean currents, hydrography and microstructure data from cruise HM2015617. https://doi.org/10.21335/NMDC-567625440

Fer, I., Nilsen, F., Baumann, T. M., Kalhagen, K., Koenig, Z., & Kolås, E. H. (2023). Ocean hydrography and current profiles from the Nansen Legacy Winter Process Cruise to the northern Barents Sea, KH2021702, February 2021 [Dataset]. University of Bergen. https://doi.org/10.21335/NMDC-1544015310

Fer, I., Peterson, A. K., & Ullgren, J. E. (2014). Microstructure measurements from an underwater glider in the turbulent Faroe Bank Channel overflow. *Journal of Atmospheric and Oceanic Technology*, *31*(5), 1128–1150. https://doi.org/10.1175/JTECH-D-13-00221.1

Fer, I., Skogseth, R., Aastad, S. S., Baumann, T. M., Elliott, F., Falck, E., et al. (2021). SS-MSC2 process cruise/mooring service 2020: Cruise Report (Tech. Rep.). https://doi.org/10.7557/nlrs.5798

Fer, I., Skogseth, R., Astad, S. S., Baumann, T. M., Elliott, F., Falck, E., et al. (2023). Ocean hydrography and current profiles from the Nansen Legacy cruise to the northern Barents Sea, GOS2020113, October 2020. https://doi.org/10.21335/NMDC-1752779505

Fer, I., Skogseth, R., & Geyer, F. (2010). Internal waves and mixing in the marginal ice zone near the Yermak Plateau. *Journal of Physical Oceanography*, *40*(7), 1613–1630. https://doi.org/10.1175/2010JPO4371.1

Fine, E. C., Alford, M. H., MacKinnon, J. A., & Mickett, J. B. (2021). Microstructure mixing observations and finescale parameterizations in the Beaufort Sea. *Journal of Physical Oceanography*, *51*(1), 19–35. https://doi.org/10.1175/JPO-D-19-0233.1

Fine, E. C., & Cole, S. T. (2022). Decadal observations of internal wave energy, shear, and mixing in the western Arctic Ocean. *Journal of Geophysical Research: Oceans*, *127*(5), 1–23. https://doi.org/10.1029/2021JC018056

Garrett, C., & Munk, W. (1972). Space-time scales of internal waves. *Geophysical Fluid Dynamics*, *3*(3), 225–264. https://doi.org/10.1080/03091927208236082

Garrett, C., & Munk, W. (1975). Space-time scales of internal waves: A progress report. *Journal of Geophysical Research*, *80*(3), 291–297. https://doi.org/10.1029/jc080i003p00291

Goto, Y., Yasuda, I., Nagasawa, M., Kouketsu, S., & Nakano, T. (2021). Estimation of Basin-scale turbulence distribution in the North Pacific Ocean using CTD-attached thermistor measurements. *Scientific Reports*, *11*(1), 1–13. https://doi.org/10.1038/s41598-020-80029-2

Gregg, M. C. (1989). Scaling turbulent dissipation in the thermocline. *Journal of Geophysical Research*, *94*(C7), 9686–9698. https://doi.org/10.1029/jc094ic07p09686

Gregg, M. C., & Kunze, E. (1991). Shear and strain in Santa Monica Basin. *Journal of Geophysical Research*, *96*(C9), 16709–16719. https://doi.org/10.1029/91jc01385

Gregg, M. C., Sanford, T. B., & Winkel, D. P. (2003). Reduced mixing from the breaking of internal waves in equatorial waters. *Nature*, *422*(6931), 513–515. https://doi.org/10.1038/nature01507

Guthrie, J. D., & Morison, J. H. (2021). Not just sea ice: Other factors important to near-inertial wave generation in the Arctic Ocean. *Geophysical Research Letters*, *48*(3), 1–10. https://doi.org/10.1029/2020GL090508

Guthrie, J. D., Morison, J. H., & Fer, I. (2013). Revisiting internal waves and mixing in the Arctic Ocean. *Journal of Geophysical Research: Oceans*, *118*(8), 3966–3977. https://doi.org/10.1002/jgrc.20294

Holloway, G., & Proshutinsky, A. (2007). Role of tides in Arctic Ocean/ice climate. *Journal of Geophysical Research*, *112*(C4), 3010–3069. https://doi.org/10.1029/2006jc003643

Ijichi, T., & Hibiya, T. (2015). Frequency-based correction of finescale parameterization of turbulent dissipation in the deep ocean. *Journal of Atmospheric and Oceanic Technology*, *32*(8), 1526–1535. https://doi.org/10.1175/JTECH-D-15-0031.1

Jakobsson, M., Mayer, L. A., Bringensparr, C., Castro, C. F., Mohammad, R., Johnson, P., et al. (2020). The International Bathymetric Chart of the Arctic Ocean Version 4.0. *Scientific Data*, *7*(1), 1–14. https://doi.org/10.1038/s41597-020-0520-9

Kunze, E., Firing, E., Hummon, J. M., Chereskin, T. K., & Thurnherr, A. M. (2006). Global abyssal mixing inferred from lowered ADCP shear and CTD strain profiles. *Journal of Physical Oceanography*, *36*(8), 1553–1576. https://doi.org/10.1175/JPO2926.1

Lenn, Y.-D., Fer, I., Timmermans, M.-L., & MacKinnon, J. A. (2022). Chapter 11 - Mixing in the Arctic Ocean. In M. Meredith & A. Naveira Garabato (Eds.), *Ocean mixing* (pp. 275–299). Elsevier. https://doi.org/10.1016/B978-0-12-821512-8.00018-9

Levine, M. D., Paulson, C. A., & Morison, J. H. (1987). Observations of internal gravity waves under the Arctic pack ice. *Journal of Geophysical Research*, *92*(C1), 779–782. https://doi.org/10.1029/JC092iC01p00779

MacKinnon, J. A., & Gregg, M. C. (2003). Mixing on the late-summer new England shelf-Solibores, shear, and stratification. *Journal of Physical Oceanography*, *33*(7), 1476–1492. https://doi.org/10.1175/1520-0485(2003)033<1476:MOTLNE>2.0.CO;2

McPhee, M. G., Kwok, R., Robins, R., & Coon, M. (2005). Upwelling of Arctic pycnocline associated with shear motion of sea ice. *Geophysical Research Letters*, *32*(10), 1–4. https://doi.org/10.1029/2004GL021819

Meyer, A., Fer, I., Sundfjord, A., & Peterson, A. K. (2016). Mixing rates and vertical heat fluxes north of Svalbard from Arctic winter to spring. *Journal of Geophysical Research: Oceans*, *122*(6), 4569–4586. https://doi.org/10.1002/2016JC012441

Meyer, A., Fer, I., Sundfjord, A., Peterson, A. K., Smedsrud, L. H., Muilwijk, M., et al. (2016). *N-ICE2015 ocean microstructure profiles (MSS90L)*. Norwegian Polar Institute. https://doi.org/10.21334/npolar.2016.774bf6ab

Nilsen, F., Fer, I., Baumann, T. M., Breivik, Ø., Czyz, C., Frank, L., et al. (2021). PC-2 winter process cruise (WPC). The Nansen Legacy Report Series(26). https://doi.org/10.7557/nlrs.6324

Nixdorf, U., Dethloff, K., Rex, M., Shupe, M., Sommerfeld, A., Perovich, D. K., et al. (2021). MOSAiC extended acknowledgement. *Zenodo*. https://doi.org/10.5281/zenodo.5179739

Padman, L., & Dillon, T. M. (1989). Thermal microstructure and internal waves in the Canada Basin diffusive staircase. *Deep-Sea Research Part A: Oceanographic Research Papers*, *36*(4), 531–542. https://doi.org/10.1016/0198-0149(89)90004-6

Padman, L., & Dillon, T. M. (1991). Turbulent mixing near the Yermak Plateau during the Coordinated Eastern Arctic experiment. *Journal of Geophysical Research*, *96*(C3), 4769–4782. https://doi.org/10.1029/90jc02260

Pinkel, R. (2008). The wavenumber-frequency spectrum of vortical and internal-wave shear in the western Arctic Ocean. *Journal of Physical Oceanography*, *38*(2), 277–290. https://doi.org/10.1175/2006JPO3558.1

Pollmann, F. (2020). Global characterization of the ocean's internal wave spectrum. *Journal of Physical Oceanography*, *50*(7), 1871–1891. https://doi.org/10.1175/JPO-D-19-0185.1

Polyakov, I. V., Pnyushkov, A. V., Alkire, M. B., Ashik, I. M., Baumann, T. M., Carmack, E. C., et al. (2017). Greater role for Atlantic inflows on sea-ice loss in the Eurasian Basin of the Arctic Ocean. *Science*, *356*(6335), 285–291. https://doi.org/10.1126/science.aai8204

Polyakov, I. V., Pnyushkov, A. V., & Carmack, E. C. (2018). Stability of the Arctic halocline: A new indicator of Arctic climate change. *Environmental Research Letters*, *13*(12), 125008. https://doi.org/10.1088/1748-9326/aaec1e

Polyakov, I. V., Rippeth, T. P., Fer, I., Baumann, T. M., Carmack, E. C., Ivanov, V. V., et al. (2020). Intensification of near-surface currents and shear in the eastern Arctic Ocean. *Geophysical Research Letters*, *47*(16), 1–9. https://doi.org/10.1029/2020GL089469

Polzin, K. L., Kunze, E., Hummon, J., & Firing, E. (2002). The finescale response of lowered ADCP velocity profiles. *Journal of Atmospheric and Oceanic Technology*, *19*(2), 205–224. https://doi.org/10.1175/1520-0426(2002)019<0205:TFROLA>2.0.CO;2

Polzin, K. L., Naveira Garabato, A. C., Huussen, T. N., Sloyan, B. M., & Waterman, S. (2014). Finescale parameterizations of turbulent dissipation. *Journal of Geophysical Research: Oceans*, *119*(2), 1383–1419. https://doi.org/10.1002/2013JC008979

Polzin, K. L., Toole, J. M., & Schmitt, R. W. (1995). Finescale parameterizations of turbulent dissipation. *Journal of Physical Oceanography*, *25*(3), 306–328. https://doi.org/10.1175/1520-0485(1995)025<0306:FPOTD>2.0.CO;2

Provost, C., Onarheim, I., Randelhoff, A., Meyer, A., Smedsrud, L.-H., Rerolle, V., et al. (2016). *N-ICE2015 ocean currents: RDI long ranger acoustic Doppler current profiler*. Norwegian Polar Institute. https://doi.org/10.21334/npolar.2017.accb9dd5

Rabe, B., Heuzé, C., Regnery, J., Aksenov, Y., Allerholt, J., Athanase, M., et al. (2022). Overview of the MOSAiC expedition: Physical oceanography. *Elementa: Science of the Anthropocene*, *10*(1), 62. https://doi.org/10.1525/elementa.2021.00062

Rainville, L., & Woodgate, R. A. (2009). Observations of internal wave generation in the seasonally ice-free Arctic. *Geophysical Research Letters*, *36*(23), 1485–1487. https://doi.org/10.1029/2009gl041291

Randelhoff, A., Holding, J., Janout, M., Sejr, M. K., Babin, M., Tremblay, J. É., & Alkire, M. B. (2020). Pan-Arctic Ocean primary production constrained by turbulent nitrate fluxes. *Frontiers in Marine Science*, *7*(March), 1–15. https://doi.org/10.3389/fmars.2020.00150

Scheifele, B., Waterman, S., Merckelbach, L., & Carpenter, J. R. (2018). Measuring the dissipation rate of turbulent kinetic energy in strongly stratified, low-energy environments: A case study from the Arctic Ocean. *Journal of Geophysical Research: Oceans*, *123*(8), 5459–5480. https://doi.org/10.1029/2017JC013731

Schulz, K., Lincoln, B., Povazhnyy, V., Rippeth, T., Lenn, Y. D., Janout, M., et al. (2022a). Increasing nutrient fluxes and mixing regime changes in the eastern Arctic Ocean. *Geophysical Research Letters*, *49*(5), 1–10. https://doi.org/10.1029/2021GL096152

Schulz, K., Mohrholz, V., Fer, I., Janout, M., Hoppmann, M., Schaffer, J., & Koenig, Z. (2022c). A full year of turbulence measurements from a drift campaign in the Arctic Ocean 2019–2020. *Scientific Data*, *9*(1). https://doi.org/10.1038/s41597-022-01574-1

Schulz, K., Mohrholz, V., Fer, I., Janout, M. A., Hoppmann, M., Schaffer, J., et al. (2022b). Turbulent microstructure profile (MSS) measurements from the MOSAiC drift, Arctic Ocean [Dataset]. PANGAEA. https://doi.org/10.1594/PANGAEA.939816

Sundfjord, A., Fer, I., Kasajima, Y., & Svendsen, H. (2007). Observations of turbulent mixing and hydrography in the marginal ice zone of the Barents Sea. *Journal of Geophysical Research*, *112*(5), 1–23. https://doi.org/10.1029/2006JC003524

Takahashi, A., & Hibiya, T. (2021). Influence of the distortion of vertical wavenumber spectra on estimates of turbulent dissipation using the finescale parameterization: Observations in the Antarctic Circumpolar Current. *Journal of Geophysical Research: Oceans*, *126*(6), e2020JC016613. https://doi.org/10.1029/2020JC016613

Takahashi, A., Hibiya, T., & Garabato, A. C. (2021). Influence of the distortion of vertical wavenumber spectra on estimates of turbulent dissipation using the finescale parameterization: Eikonal calculations. *Journal of Physical Oceanography*, *51*(5), 1723–1733. https://doi.org/10.1175/JPO-D-20-0196.1

Thomas, L., & Zhai, X. (2021). The lifecycle of surface-generated near-inertial waves. In M. Meredith & A. Garabato (Eds.), *Ocean mixing - Drivers, mechanisms and impacts* (pp. 95–115). Elsevier. https://doi.org/10.1016/B978-0-12-821512-8.00012-8

Timmermans, M. L., & Marshall, J. (2020). Understanding Arctic Ocean circulation: A review of ocean dynamics in a changing climate. *Journal of Geophysical Research: Oceans*, *125*(4), 1–35. https://doi.org/10.1029/2018JC014378

Turner, J. S. (2010). The melting of ice in the Arctic Ocean: The influence of double-diffusive transport of heat from below. *Journal of Physical Oceanography*, *40*(1), 249–256. https://doi.org/10.1175/2009JPO4279.1

Whalen, C. B. (2021). Best practices for comparing ocean turbulence measurements across spatiotemporal scales. *Journal of Atmospheric and Oceanic Technology*, *38*(4), 837–841. https://doi.org/10.1175/JTECH-D-20-0175.1

Whalen, C. B., MacKinnon, J. A., Talley, L. D., & Waterhouse, A. F. (2015). Estimating the mean diapycnal mixing using a finescale strain parameterization. *Journal of Physical Oceanography*, *45*(4), 1174–1188. https://doi.org/10.1175/JPO-D-14-0167.1

Yasuda, I., Fujio, S., Yanagimoto, D., Lee, K. J., Sasaki, Y., Zhai, S., et al. (2021). Estimate of turbulent energy dissipation rate using free-fall and CTD-attached fast-response thermistors in weak ocean turbulence. *Journal of Oceanography*, *77*(1), 17–28. https://doi.org/10.1007/s10872-020-00574-2